Chemical Engineering Journal 525 (2025) 168691

Contents lists available at ScienceDirect

Chemical Engineering Journal

journal homepage: www.elsevier.com/locate/cej

Evaluation of key operational parameters in a novel pilot-scale rotating disk bioelectrochemical reactor for hydrogen production in a wastewater biorefinery

Nikhil Shylaja Prakash [a], Willow Neske [b,d], Max Rümenapf [b], Zhizhao Xiao [b], Andreas Netsch [a,b], Harald Horn [a,b], Jonas Ullmann [a], Johannes Eberhard Reiner [b,c], Andrea Hille-Reichel [a,b,*]

[a] DVGW Research Centre, Water Chemistry and Water Technology, Engler-Bunte-Ring 9a, 76131, Karlsruhe, Germany
[b] Engler-Bunte-Institut, Water Chemistry and Water Technology, Karlsruhe Institute of Technology (KIT), Engler-Bunte-Ring 9a, 76131, Karlsruhe, Germany
[c] The Novo Nordisk Foundation CO_2 Research Center - CORC - iNano, Gustav Wieds Vej 10, 3130, 212, 8000, Aarhus C, Denmark
[d] Department of Biological and Environmental Engineering, Cornell University, Ithaca, NY, 14853, United States

ARTICLE INFO

Keywords:
Rotating disk bioelectrochemical reactor
Microbial electrolysis
Wastewater biorefinery
Biohydrogen
Biohythane
Short-chain fatty acids

ABSTRACT

Within the context of a wastewater biorefinery (WWBr), hydrolyzed sludge containing short-chain fatty acids (SCFAs) holds significant potential for bio-valorization. In this study, a custom-designed single chamber 100-L rotating disk bioelectrochemical reactor (RDBER) was evaluated as a terminal treatment step in a WWBr for hydrogen production. The RDBER features rotating circular anodes with a high anodic area to reactor volume ratio (100 m^2 per m^3). During start-up, the reactor was inoculated with *Shewanella oneidensis* and *Geobacter sulfurreducens*, with the latter serving as the primary exoelectrogen for substrate oxidation. The reactor was operated for 200 days in batch and continuous modes to optimize pH, hydraulic retention time (HRT), ionic conductivity, recirculation rate, rotational speed, and anode potential. The batch mode was operated with the defined dual-species culture in a sterilized medium, whereas in the continuous mode, unsterilized hydrolyzate with SCFAs was utilized. In the batch phase, a methane-free gas phase with high H_2-fraction (80 %) was maintained for 130 days. Under these conditions, current density peaked and stabilized at 240 $mA \bullet m_{anode}^{-2}$, achieving a Coulombic efficiency (CE) of 70 %, and a maximum of 36 L $H_2 \bullet m_{reactor}^{-3} \bullet d^{-1}$ was harvested. Among the operational parameters tested in batch mode, a threefold increase in recirculation rate improved current density by 100 %. Following the batch period, continuous feeding was initiated, and the reactor transitioned towards biohythane production (9 % H_2 / 86 % CH_4). At an HRT of 3 days, current density amounted to 170 $mA \bullet m_{anode}^{-2}$ (CE ≈ 33 %), while yielding 3 L $H_2 \bullet m_{reactor}^{-3} \bullet d^{-1}$ and 33 L $CH_4 \bullet m_{reactor}^{-3} \bullet d^{-1}$. Gravimetric and image analyses revealed an annular biofilm distribution covering only one-third of the anode area. Limited mass transfer due to close arrangement of the anode disks was identified to be a major factor impeding reactor performance. Further optimization of the reactor architecture and its hydrodynamics is proposed to notably enhance the RDBER's bioelectrochemical performance.

1. Introduction

Within the context of a circular economy, wastewater treatment plants (WWTPs) have gained increasing interest as valuable sources for energy recovery [1]. Biogas is the typical energy carrier generated from WWTPs during the anaerobic digestion of sludge. However, the need for sustainable energy sources has shifted focus towards greener fuels like hydrogen due to its cleaner combustion profile [2].

Bioelectrochemical systems (BES), specifically microbial electrolysis cells (MEC), are a promising technology to harvest biohydrogen from waste streams containing short-chain fatty acids (SCFAs) [3–5]. MECs rely on electroactive microorganisms, for instance, *Geobacter* sp., which can utilize solid electrodes as terminal electron acceptors for their respiratory energy gain. In nature, the bacteria would use, e.g., iron minerals as electron acceptors, whereas in technical applications, they transfer electrons from the oxidation of easily degradable carbon sources like SCFAs to an electrode poised at an oxidative potential via

* Corresponding author at: Karlsruhe Institute of Technology (KIT), Engler-Bunte-Institut, Water Chemistry and Water Technology, Engler-Bunte-Ring 9a, 76131, Karlsruhe, Germany.
E-mail address: andrea.hille-reichel@kit.edu (A. Hille-Reichel).

https://doi.org/10.1016/j.cej.2025.168691
Received 2 June 2025; Received in revised form 21 August 2025; Accepted 18 September 2025
Available online 22 September 2025

Abbreviations

BES	Bioelectrochemical system
COD	Chemical oxygen demand
CFD	Computational fluid dynamics
DO	Dissolved oxygen
EtOH	Ethanol
HAc	Acetic acid
HBu	Butyric acid
HBu-iso	Iso-butyric acid
HPr	Propionic acid
HVa	Valeric acid
HVa-iso	Iso-valeric acid
ME	Margin of error
MEC	Microbial electrolysis cell
OCT	Optical coherence tomography
PFAS	*per-* and polyfluoroalkyl substances
RDBER	Rotating disk bioelectrochemical reactor
RME	Relative margin of error
SCFAs	Short-chain fatty acids
sCOD	Soluble chemical oxygen demand
SHE	Standard hydrogen electrode
SI	Supplementary information
WWBr	Wastewater biorefinery
WWTP	Wastewater treatment plant

Symbols

BA_{eff}	Effective biofilm area m^2
BV	Biovolume $\mu m^3 \bullet \mu m^{-2}$
CE	Coulombic efficiency %
DO	Dissolved oxygen $mg \bullet L^{-1}$
$E_{anode,\ app}$	Applied potential at the anode mV
F	Faraday constant $C \bullet mol^{-1}$
I	Current mA
J	Current density $mA \bullet m^{-2}$
m_N	Normalized biomass $g \bullet m^{-2}$
N	Number of anode disks –
n	Number of vertices –
n_{e^-}	Number of electrons –
rpm	Rotation per minute –
SC	Substrate coverage %
SC_{eff}	Effective surface coverage %
σ	Standard deviation –
μ	Average –
V_B	Biofilm volume μm^3
$V_{CH4,\ harv}$	Methane harvested $L \bullet m^{-3}_{reactor} \bullet d^{-1}$
$V_{H2,\ th}$	Theoretical hydrogen production $L \bullet m^{-3}_{reactor} \bullet d^{-1}$
$V_{H2,\ th}$	Theoretical hydrogen production $L \bullet m^{-3}_{reactor} \bullet d^{-1}$

extracellular electron transfer, generating an anodic current [1]. The anode potential generated from the oxidation of an easily degradable carbon source like acetate is around −300 mV (vs standard hydrogen electrode (SHE)), and the reversible potential of H^+/H_2 is around −414 mV. This means that a minimum theoretical voltage of 114 mV is required for hydrogen evolution at the cathode, which is significantly lower than the theoretical voltage of 1.23 V required for water electrolysis [6,7]. This makes MEC an attractive choice for hydrogen recovery in comparison to conventional electrolysis.

Typical reactor configuration for MECs are single and double chamber systems [8]. Double chamber MECs, separated by semi-permeable membranes, can enhance hydrogen recovery [9]. However, semi-permeable membranes can cause proton accumulation in the anode chamber leading to unfavorable pH conditions for electroactivity [10]. In addition, membranes can cause additional internal resistances (resulting in ohmic losses), and undergo fouling [11]. Moreover, *per-* and polyfluoroalkyl substances (PFAS)-based proton exchange membranes are commonly used in MECs due to their high proton conductivity [12]. The risk of PFAS leakage and the potential risks and toxicity it poses to the environment are major concerns that require consideration during a full-scale implementation [12]. In comparison, scaling up single chamber MECs is practical from an economic standpoint due to its simpler design [9,13]. However, single chamber MECs pose a risk in terms of reduced hydrogen recoveries due to consumption by hydrogen scavengers [14]. Considering the trade-off between membrane-related challenges in double chamber MECs and the lower hydrogen recoveries but a practical scalability of single chamber MECs, the question remains: which configuration is better suited for scalable and sustainable biohydrogen production?

Research on scale-ups (in the 100-L range) of MECs focused mostly on double chamber setups [8,14–16,18–22], with the exception of a 1000-L single chamber MEC used by Cusick et al. [14]. These pilot-scale studies on single and double chamber MECs have used the so-called modular or "cassette-type" configuration with several serially arranged electrode modules. With this arrangement, the range of anodic/volumetric current densities for double chamber pilot-scale MECs has been reported to be around 200 to 2,000 $mA \bullet m^{-2}_{anode}$ or 340 to 16,000 $mA \bullet m^{-3}_{reactor}$, while hydrogen production is in the range of 3 to 200 L $H_2 \bullet m^{-3}_{reactor} \bullet d^{-1}$ [8,14–16,18–22]. With the single chamber pilot-scale MEC [14], the reported volumetric current density was around 8,000 $mA \bullet m^{-3}_{reactor}$ (anodic current density was not reported), while the maximum hydrogen production was around 100 L $H_2 \bullet m^{-3}_{reactor} \bullet d^{-1}$.

Despite considerable successful attempts at scale-ups, the "cassette-type" configuration employed in most research is a numbering-up strategy — increasing the number of smaller modules to have more treatment area. Such a modular expansion does not represent a true geometric scale up from an engineering standpoint, which is actually realistically required when a large electrode area for biofilm growth is required for treating larger wastewater pollutant loads. Increasing the number of small-sized electrode modules poses disadvantages in terms of larger footprints and huge costs for operating individual modules [15,23], making it economically challenging.

Therefore, there is a niche within the scope of scaling up bioelectrochemical systems to develop a reactor that has a large surface-area-to-volume ratio to enable efficient treatment within a compact footprint. Based on our literature research on pilot-scale setups, the highest anode area to reactor volume ratio (or specific anode area) reported was 34 $m^2_{anode} \bullet m^{-3}_{reactor}$ [16], with the rest of the pilot-scale MECs being in the range of 7 to 22 $m^2_{anode} \bullet m^{-3}_{reactor}$ [8,14,16,18–22]. Clearly, there is a notable opportunity to optimize MECs in terms of architecture and operability.

To address the issue of spatial demand and operational feasibility, our study introduces a novel 100-L rotating disk bioelectrochemical reactor (RDBER). The reactor, engineered by Max Hackbarth based on a bench-scale model [24], is modeled after the design configuration of a rotating biological contactor (RBC) [25]. The main advantages of the RBC are the reduced operational costs and the smaller footprint. The use of rotating disks to enhance substrate uptake is energy efficient while the closely spaced rotating disks offer a high surface area reducing space requirements. The RDBER builds upon the advantages of the RBC while incorporating microbial electrolysis. The RDBER is characterized by the lack of a membrane separator between the electrodes (single chamber) and a high specific anode area (100 $m^2_{anode} \bullet m^{-3}_{reactor}$) owing to the closely spaced rotating anodes [26].

Considering the fact that only one single chamber MEC has been operated at pilot-scale [14], and there is little information on how single

chamber MECs compete with double chamber MECs in terms of geometric scale-up — as opposed to modularization — this study employs a single chamber RDBER at pilot-scale for the first time. This work aims at systematic long-term evaluation of the RDBER and its contextualization among pilot-scale MECs. The proof of concept of the reactor was assessed as a terminal treatment step to produce hydrogen in a wastewater biorefinery (WWBr). Within the purview of the WWBr concept, sewage sludge is anaerobically fermented to produce high concentrations of SCFAs. The SCFAs are then separated from the sludge through microfiltration into a particle-free hydrolyzate which can be readily used as substrate for microbial electrolysis for hydrogen/biofuel recovery [27].

Two RDBERs were evaluated in this work, one under controlled laboratory conditions, and the other on-site at a WWTP. The laboratory-controlled RDBER was operated for 200 days and was first experimented in a defined dual-species batch mode with a sterile medium to optimize crucial operational parameters such as rotational speed of the anode, recirculation rates of the reactor medium, ionic conductivity, and applied anodic potential. After optimization, feeding was switched to continuous mode (under unsterile conditions) with the microfiltered hydrolyzate containing SCFAs. Additional parameters like hydraulic retention time and pH were tested in the continuous mode. Also, the reactor was assessed for potential limitations and improvements in design by analyzing the pattern of biofilm development on the rotating anodes via image and gravimetric analyses. The RDBER operated on-site at a WWTP under unsterile conditions was compared for performance but was not subject to detailed assessment. Finally, to position the RDBER within the class of existing pilot-scale MEC reactors, the optimum performance was compared in terms of anodic and volumetric current density and hydrogen production.

2. Materials and methods

2.1. Experimental setup

The presented research mainly focuses on the laboratory-controlled RDBER. The RDBER operated on-site at a WWTP in a completely unsterile condition was mainly compared for performance.

The cross-sectional scheme and photographic representations of the 100 L-RDBER (working volume = 90 L) can be found in Fig. 1A and C, respectively. The specific anodic area was 100 m^2 anode area per m^3 of reactor volume or 111 m^2 anode area per m^3 of working volume. The corpus of the reactor including the gastrap were made out of polypropylene. A threaded titanium shaft, placed centrally, along the length of the reactor frame supported the anodes and also acted as a current collector. The circular anode disks (working electrode) were stacked on the shaft separated by titanium nuts (see the arrangement of anode disks along axial direction x in Fig. 1A and the photographical depiction in Fig. 1D). A total of 65 anode disks (material: graphite polymer composite material, thickness: 3 mm, diameter = 33 cm, Whitecell Eisenhuth GmbH & Co. KG, Osterode, Germany) spaced 1.2 cm apart, amounted to a total effective area of 10 m^2. The anode disks each had three holes that were axially distributed to improve advective liquid transport along the reactor length (see Fig. 1B). The holes of each anode disk was ensured not to align with those of the subsequent disk. The diameter of the each hole was 2.8 cm. This diameter was chosen arbitrarily to facilitate advective liquid transport — small enough to maintain sufficient flow but not too large to reduce anodic area. The anodes mounted on the titanium rod were connected to a high-resolution stepping motor (Lexium Mdrive Motion Control, Schneider Electric), with which the rotational speed of the anode was controlled. The counter electrode, i.e., the perforated stainless steel cathode, shaped as a half cylinder with supports on either side, was placed over the anodes (see Fig. 1B and Fig. 1D). This cathodic configuration mimics a bench-scale RDBER [24] modified from an earlier bench-scale design with semi-circular cathode disks arranged closely between the anodes [27]. This change in design was carried out to reduce reoxidation of hydrogen at the cathode and improve recovery of the same. The cathode area was approximately 0.99 m^2. An Ag/AgCl reference electrode (SE23I, Meinsberg Sensortechnik) was placed at the midpoint of the reactor submerged in the reactor medium (Fig. 1A). A potentiostat (Interface 5000P, Gamry Instruments, USA) was used to control the anodic potential. A gear pump (Masterflex, Ismatec, Germany) was used to mix the reactor medium by creating a flow via recirculation of the liquid phase. A peristaltic pump (Rotarus®, Hirschmann Laborgeräte GmbH & Co. KG, Eberstadt, Germany) was used to feed the reactor during continuous operation. The volumetric flow rate of the gas leaving the headspace of the gastrap was measured using a drum type gas flow meter (Ritter Apparatebau GmbH, Germany). An electrical silicone heating mat (LCS IsoTherm GmbH & Co. KG, Frankfurt am Main, Germany) was used to insulate the reactor and maintain a constant temperature range over the course of the experiment (see Table 1 in Section 2.8 for exact temperature values).

2.2. Preculture and inoculation

Preculture and inoculation were done according to Hackbarth et al. [24]. During operation, a mixed culture of *Shewanella oneidensis* MR-1 [28] and *Geobacter sulfurreducens* PCA [29] as the biocatalysts was used in the RDBER. *S. oneidensis* was aerobically precultured in Luria-Bertani medium (Lennox), while *G. sulfurreducens* was anaerobically grown in a BES medium according to [30]. *S. oneidensis* and *G. sulfurreducens* were then inoculated in the reactor at a ratio of 9:1 (initial optical density (OD_{600}) = 0.1). Separately, *Desulfuromonas acetexigens* 2873 (DSMZ 1397) was also anaerobically grown in the BES medium and introduced at a later stage of the experiment.

A detailed description of the BES medium composition and inoculation procedure can be found in SI *section 1.1*. It is important to mention that the inoculation procedure described in SI *section 1.1* was also followed for the RDBER operated on-site under unsterile conditions, but was not inoculated with *D. acetexigens* at any point.

2.3. Sterilized start-up and reactor anaerobization

Prior to the introduction of the inoculated medium, the laboratory-controlled RDBER underwent two steps of chemical sterilization with hydrogen peroxide (H_2O_2) and ethanol (EtOH) to prevent the introduction or growth of an unintended microbial community that could hinder the reactor performance, and also to ensure the dominance of the specific electroactive strains in the biofilm matrix. Hydrophobic polytetrafluoroethylene (PTFE) membranes with a pore size of 0.2 μm were used at all open-to-atmosphere exit points during the defined dual-species operational period. Details to the sterilization procedure can be found in SI *section 1.2*. Following the two-step sterilization, 90 L of anaerobized inoculated BES medium with 25 mM acetate and 25 mM lactate as carbon sources was pumped into the reactor. Due to incomplete drainage of etOH, a notable concentration of EtOH along with acetate and lactate was present as an additional carbon source. In contrast, the RDBER operated on-site did not undergo any form of sterilization prior to the start-up.

2.4. Hydrolyzate preparation

The RDBER is intended to be used as a terminal treatment step in a wastewater biorefinery to valorize SCFAs into hydrogen. SCFAs are obtained from the anaerobic fermentation of primary sludge; the SCFAs are then recovered via a two-step membrane separation method [27]. The first filtration step is a chamber filter-press characterized by a mesh size of 100 μm, whose filtration efficiency was aided by a cationic starch-based flocculant (hydroxypropyl trimethyl ammonium starch, HPAS, HKF CleanTech AG, Switzerland). The second filtration step is microfiltration (Atec, Ulm, Germany) with a ceramic membrane having pore

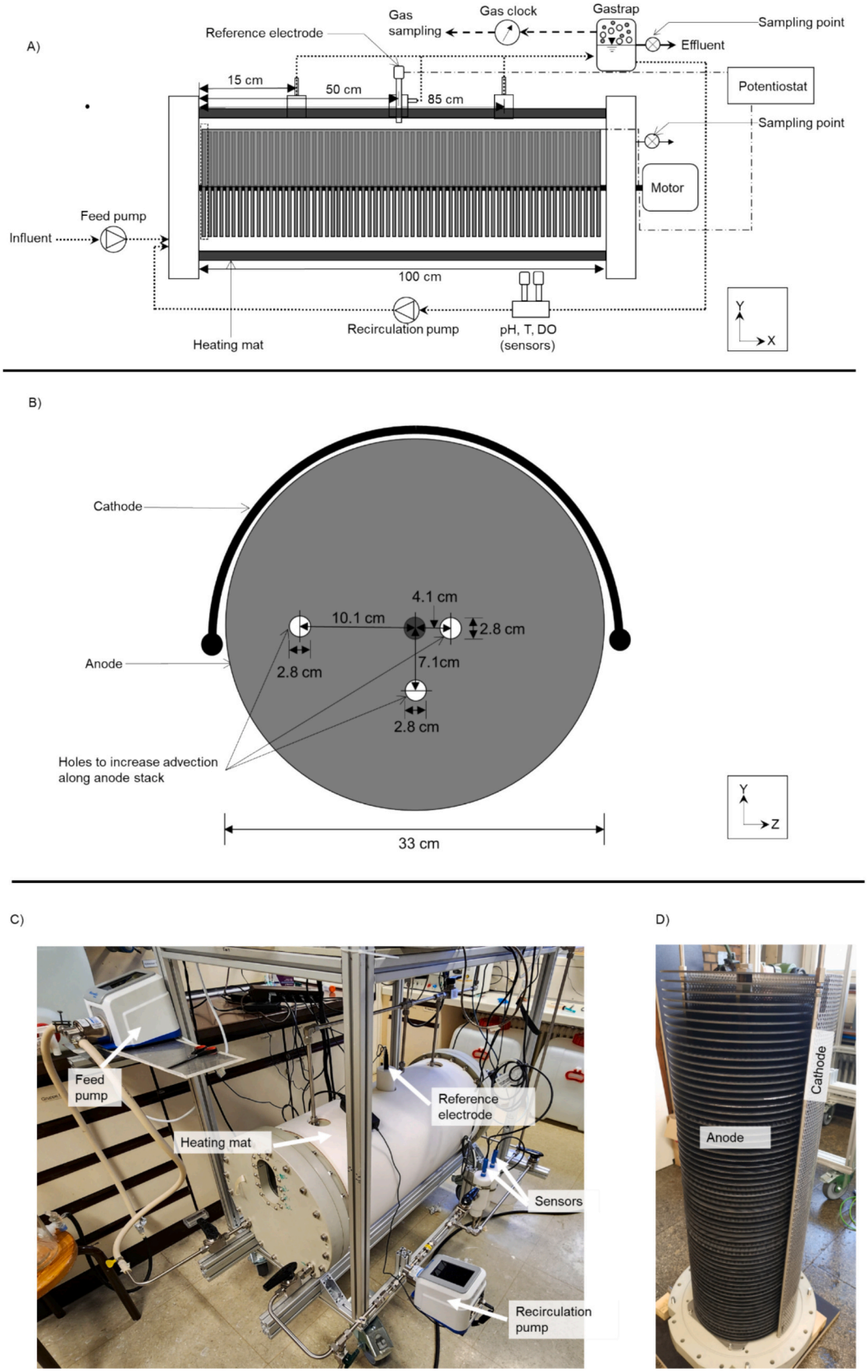

Fig. 1. A) Cross-sectional scheme of the 100-L RDBER, B) Cross-sectional view of the electrodes, C) Photograph of the 100-L RDBER, D) Photograph showing the anodes stacked on the titanium shaft. The perforated stainless steel cathode shaped as a half-cylinder extends over the length of the stack of anode disks. Note: DO represents dissolved oxygen; in Section 3.4, the spatial arrangement of anodes is crucial to analyze biofilm distribution. Disks facing the axial direction x represents the leading (front) side, while disks facing away from axial direction -x represents the trailing (rear) side.

Table 1
Specific description of phases during the operation of the RDBER (recirculation rate is presented as h^{-1} (i.e., recirculation rate ($m^3 \bullet h^{-1}$)/reactor volume (m^3). Note: see SI Fig. 2 for a complete overview. Note: The temperature was maintained within a constant range between days 3 and around 130 (Table 1). However, starting from day 130, the seasonal variation in temperature led to significant temperature shifts between the day and night cycle (see SI Fig. 2 and SI Table 1 for variation in temperature). The underlined parameters were fixed during a particular phase to monitor the response of the system to the change in the targeted parameter. The targeted parameter is highlighted in bold and underlined.

Phases	Description and objective	Period (d)	Mode	HRT (d)	pH	T (°C)	Rotational speed of anode (rpm)	Recirculation rate (h^{-1})	$E_{anode,\ app}$ (mV vs SHE)
Phase I: start-up	1) The reactor was inoculated with *G. sulfurreducens* and *S. oneidensis* on day 0 2) Observing the initial adaptation phase of electroactive bacteria (day 0 to day 12) 3) Response of electroactivity to change in pH and ionic conductivity (day 12 to day 30)	0 to 12	Batch	–	*	*	*	*	*
		12 to 30	Batch	–	7.2 ± 0.2	29.8 ± 0.2	1	0.9	300
phase II: effect of applied anodic potential before and after dilution with anaerobized sterile demineralized water	1) Between days 31 and 41, the anodic potential ($E_{anode,\ app}$) was varied to understand, if lowered potential significantly affected electroactivity 2) On day 41, the RDBER medium was diluted with anaerobized demineralized water. This was done as there was production of acetate within the system until day 41 (explained in ***section 3.1.4***). Following dilution, the system was assessed for performance due to increased internal resistance and potential biofilm sloughing 3) The impact of $E_{anode,\ app}$ before and after dilution was evaluated. **Note:** the start-up phase I (days 12 to 30) is also included in the comparison with phase II, as days 31 to 41 are a continuation of phase I prior to dilution	12 to 30	Batch	–	7.2 ± 0.2	29.8 ± 0.2	1	0.9	**300**
		31 to 38	Batch	–	6.9	29.8 ± 0.2	1	0.9	**200**
		38 to 41	Batch	–	6.9	29.8 ± 0.2	1	0.9	**100**
		41 to 47	Batch	–	7.5 ± 0.1	29.9 ± 0.8	1	0.9	**100**
		47 to 52	Batch	–	7.5 ± 0.1	29.9 ± 0.8	1	0.9	**0**
		52 to 60	Batch	–	7.5 ± 0.1	29.9 ± 0.8	1	0.9	**300**
phase III: effect of applied anodic potential before and after dilution with sterilized (autoclaved-microfiltered) hydrolyzate	1) On 4 days between days 60 and 72, 11 % RDBER medium was replaced with sterilized (autoclaved-microfiltered) hydrolyzate (i.e., four dilutions) — see SI Table 1 for composition 2) Firstly, the effect of dilution with the hydrolyzate was evaluated. Days 52 to 60 (a part of phase II) was included for comparison as it represents the time before dilution with the sterilized hydrolyzate 3) To improve upon electroactivity after dilution, $E_{anode,\ app}$ was stepped up between days 74 and 82 and assessed	52 to 60	Batch	–	7.5 ± 0.1	29.9 ± 0.8	1	0.9	**300**
		60 to 72	Batch	–	7 ± 0.1	29.7 ± 0.1	1	0.9	**300**
		73 to 74	Batch	–	7 ± 0.1	29.7 ± 0.1	1	0.9	**300**
		74 to 76	Batch	–	7 ± 0.1	29.7 ± 0.1	1	0.9	**400**
		76 to 80	Batch	–	7 ± 0.1	29.7 ± 0.1	1	0.9	**500**
		80 to 82	Batch	–	7 ± 0.1	29.7 ± 0.1	1	0.9	**600**
phase IV: impact of disk rotation and recirculation rates on hydrodynamics	1) Suspecting low substrate diffusion, firstly, the rotational speed was increased. **Note:** days 80 to 82 (a part of phase III) was included as the conditions are similar. Rotational speed was optimized until day 87 2) Later, to enhance substrate transport by bulk liquid movement, the recirculation rates were increased. **Note:** days 84 to 87 was included for comparison of recirculation rates as all other conditions are similar	80 to 82	Batch	–	7 ± 0.1	29.7 ± 0.1	**1**	0.9	600
		82 to 84	Batch	–	7.3 ± 0.1	30.5 ± 0.5	**1.2**	0.9	600
		84 to 87	Batch	–	7.3 ± 0.1	30.5 ± 0.5	**1.4**	0.9	600
		84 to 87	Batch	–	7.3 ± 0.1	30.5 ± 0.5	1.4	**0.9**	600
		87 to 90	Batch	–	7.3 ± 0.1	30.5 ± 0.5	1.4	**1.9**	600
		90 to 91	Batch	–	7.3 ± 0.1	30.5 ± 0.5	1.4	**2.8**	600
		91 to 96	Batch	–	7.3 ± 0.1	30.5 ± 0.5	1.4	**3**	600
phase V: influence of ionic conductivity on internal resistance	1) To reduce internal resistance in the RDBER, the medium was spiked twice (on days 96 and 103) with 3.4 M KCl 2) Days 91 to 96 (from phase IV) was included for comparison prior to change in ionic conductivity as the all other conditions are similar	91 to 96	Batch	–	7.3 ± 0.1	30.5 ± 0.5	1.4	3	600
		96 to 103	Batch	–	7.5 ± 0.1	30.4 ± 0.5	1.4	3	600
		103 to 110	Batch	–	7.5 ± 0.1	30.4 ± 0.5	1.4	3	600

(*continued on next page*)

Table 1 (*continued*)

Phases	Description and objective	Period (d)	Mode	HRT (d)	pH	T (°C)	Rotational speed of anode (rpm)	Recirculation rate (h^{-1})	$E_{anode,\ app}$ (mV vs SHE)
Between phases V and VI	1) Inoculation with *Desulfuromonas acetexigens* on day 110. The days that followed this were to evaluate impact of *D. acetexigens* on electroactivity 2) To enhance substrate diffusion for *D.acetexigens*, disk rotation increased to 2 rpm and 3 rpm 3) Unsterilized particle-free synthetic hydrolyzate (10*L*) was introduced on days 135 and 136 before continuous feeding began in phase VI (day 149). The two-time unsterile dilution was performed to observe if there was an onset of methanogenesis. **Note**: The synthetic hydrolyzate mimics the composition of the actual hydrolyzate (see **SI Table 1**)	110 to 125	Batch	–	7.5 ± 0.2	30.3 ± 0.7	**1.4**	3	600
		125 to 130	Batch	–	7.5 ± 0.2	30.3 ± 0.7	**2**	3	600
		130 to 149	Batch	–	7.5 ± 0.2	30.3 ± 0.7	**3**	3	300
phase VI: continuous feeding of particle-free unsterilized synthetic hydrolyzate	1) In phase VI, synhetic hydrolyzate was used (see **SI Table 1** for composition). The hydrolyzate was particle-free 2) The aim was to assess if shorter HRTs could result in washout of methanogens 3) The pH was increased to slightly alkaline range to suppress methanogenesis	149 to 159	Conti.	**3.4 ± 0.3**	**8.4 ± 0.3**	31.2 ± 0.7	3	3	300
Between phases VI and VII	1) Due to significant occurrence of methanogenesis in phase VI, the pH was made highly alkaline (around 8.9) to suppress the same 2) As highly alkaline pH affected electroactivity, the pH was slightly reduced in the subsequent phase	159 to 179	Batch	–	**8.9 ± 0.1**	32.2 ± 0.2	3	3	300
phase VII — **Phase VII (A)**	1) In phase VII, real hydrolyzate was used (see **SI Table 1** for composition). The hydrolyzate was not particle-free due to long-term storage under unsterile conditions 2) Phase VII is split into two phases, VII (A) and VII (B) 3) Phase VII (A) (between days 179 and 190), the HRT was increased, and the pH was less alkaline 4) In phase VII (B) (between days 191 and 200), the HRT was further increased, and the pH was made more alkaline due to increased methanogenesis	179 to 190	Conti.	**6.7 ± 2.8**	**7.9 ± 0.1**	32.2 ± 1.2	3	3	300
phase VII — **Phase VII (B)**		191 to 200	Conti.	**8.6 ± 2.5**	**8.6 ± 0.1**	32.2 ± 1.2/]	3	3	300

* subject to variation—explained in subsequent ***section 3.1.1*** and ***3.1.3***, Conti. stands for continuous.

size of 0.2 μm (Inopor, Germany), and hence the final product is a particle-free hydrolyzate containing predominantly SCFAs. It is important to mention that the hydrolyzate obtained after microfiltration underwent long-term unsterile storage which resulted in the formation of flocs (agglomerated particles).

For the batch phase (discussed in Section 3.1.5), the microfiltered hydrolyzate was again microfiltered (0.2 μm) with a vacuum filtration setup to render it particle-free. The two-time microfiltered hydrolyzate was then autoclaved and used in the batch phase. For the continuous phase (described in Section 3.2), the hydrolyzate obtained after the ceramic microfiltration was directly fed along with particles. The detailed composition of the hydrolyzate can be found in SI Table 1. For the RDBER operated on-site, the description of the hydrolyzate used under unsterile conditions can be found in SI Fig. 11.

2.5. Analytical methods

Dissolved oxygen (DO) and pH sensors (Endress and Hauser, Germany) were installed in the recirculation line (see Fig. 1A). The electrodes were integrated with temperature sensors. Electric conductivity was measured offline with a portable multimeter (WTW Multi 350i, Xylem, USA). Electric conductivity was measured offline (after taking liquid samples) with a portable multimeter (WTW Multi 350i, Xylem, USA). Liquid samples were collected from the sampling points (see Fig. 1A) during batch and continuous modes to quantify SCFAs (mainly acetic (HAc), propionic (HPr), butyric (HBu), isobutyric (HBu-iso), valeric (HVa), isovaleric (HVa-iso) acids) and lactic acid (HLa)) after filtration with a 0.45 μm polyether sulfone filter (Sterlitech Corporation, USA) using Metrohm 881 Compact Pro Ion Exchange Chromatograph with a Metrosep Organic Acids 250/7.8 column (Metrohm, Switzerland). The liquid samples, again after filtration, were also tested for soluble chemical oxygen demand (sCOD) using quick tests (LCK 514, Hach Lange, Germany). HAc and HLa are supposedly expected to be the main carbon sources in the reactor, however, leftover EtOH after sterilization (as described in Section 2.3) was present as an additional carbon source. Only the initial sample was quantified for EtOH using a gas chromatograph coupled with a flame ionization detector (Agilent 7890B, USA). Following samples were quantified by subtracting the COD equivalence of SCFAs from the total sCOD, and expressed in terms of molarity (expressed as $sCOD_{rest}$). This type of quantification was done only until the point of introduction of the hydrolyzate into the reactor. Gas samples were collected at the outlet of the gas clock and the gas composition was measured using a Micro GC (490 Micro GC, Agilent Technologies, Germany). Volume of the gas recorded by the gas clock at 5-min intervals was normalized using Rigamo software (Ritter Apparatebau GmbH, Germany).

Illumina sequencing was used to analyze the microbial community composition in the reactor, and samples were taken from the planktonic phase, anodic and cathodic biofilm. Samples were analyzed at private Institute for Molecular Analytics Karlsruhe GmbH (IMA, Germany). Brief explanation to the sequencing can be found in SI *section 1.4*. Samples to analyze microbial community in the planktonic phase were taken between day 97 and 105, day 116 and day 200 (after termination of the experiment). Samples from the anodic and cathodic biofilms were taken on day 200 (after termination of the experiment). Microbial community analysis was not carried out for the RDBER operated on-site.

The performance of the laboratory-controlled RDBER was evaluated by analyzing the biofilm distribution on the anodes after the experimental period. After deconstruction of the RDBER, the anodic biofilm distribution was assessed from the selected anode disks. The parameters analyzed were 1) normalized biomass (m_N), 2) mean biovolume ($\overline{BV}$), 3) substratum coverage (SC), and 4) effective substratum coverage (SC_{eff}). m_N ($g \bullet m^{-2}$) represents the mass of scraped biomass (g) normalized to the individual anode area (m^2). $\overline{BV}$ ($m^3 \bullet m^{-2}$) and SC (%) are biofilm parameters obtained from optical coherence tomography [31]. $\overline{BV}$ is representative of the area-related biofilm volume and thus often a good estimate of biofilm thickness, and SC shows the site-specific coverage of biofilm for a specified anode area. SC_{eff} is similar to SC, but uses the entire anode area. m_N, $\overline{BV}$ and SC are measured for specific disks, while SC_{eff} is measured for all. A detailed description of the parameters and the methods used can be found in SI *section 1.5*.

2.6. Data interpretation

Average current density j ($mA \bullet m^{-2}$) was calculated using the following equation,

$$j = \left[\frac{\int_{t_i}^{t_f} I \bullet dt}{t_f - t_i}\right] \bullet \left[\frac{1}{A_{anode,tot}}\right] \quad (i)$$

where, I (mA) is the current produced (recorded every 300 s) and $A_{anode,tot}$ (m^2) is the total area of the anodes. t_i and t_f are the initial and final time stamps (d), respectively, that represent the operational period of a particular phase.

The Coulombic efficiency CE (%) for a particular phase was evaluated accordingly,

$$CE = \left[\frac{\int_{t_i}^{t_f} I \bullet dt}{n_{e^-} \bullet \Delta c \bullet V_W \bullet F}\right] \times 100 \quad (ii)$$

where, I (mA) is the current produced over a specific period in a phase, and n_{e^-} is the number of electrons released from the consumption of 1 mol of a specific carbon source. For HAc, HPr, HBu-iso, HBu, HVa-iso and HVa, the number of electrons per mole is 8, 14, 20 and 26 mol of electrons (see SI Table 5), respectively. If CE is calculated based on COD, then the number of moles of electrons released per gram of COD consumed is 0.125 (SI Table 5). Δc (M) is the actual change in molar concentration (due to consumption) of a specific carbon source or COD and V_W (L) is the working volume. F is the Faraday constant ($96{,}485 C \bullet mol^{-1}$).

Average theoretical hydrogen production $V_{H2,th}$ ($NL \bullet d^{-1}$) is calculated based on the current produced,

$$V_{H_2,th} = \left[\frac{\int_{t_i}^{t_f} I \bullet dt}{t_f - t_i}\right] \bullet \left[\frac{R \bullet T}{F \bullet y_{e^-} \bullet p}\right] \quad (iii)$$

where, y_{e^-} is the yield of electrons (2 mol of electrons per mole of H_2), p the atmospheric pressure (1 atm), R universal gas constant ($0.082 atm \bullet L \bullet mol^{-1} \bullet K^{-1}$) and T the temperature (273 K), respectively.

Based on the fraction of gas (H_2, CH_4) determined by Micro GC, the average daily production of hydrogen and methane harvested from the reactor $V_{H2/CH4,harv}$ ($NL \bullet d^{-1}$) was calculated as follows,

$$V_{H_2/CH_4,harv} = \frac{\int_{t_i}^{t_f} V_{H_2/CH_4,harv} \bullet dt}{t_f - t_i} \quad (iv)$$

2.7. Statistical data validation

2.7.1. Continuous measurements

The 200-day experiment was separated into several phases, where each phase describes the evaluation of a particular parameter (see Section 2.8). For continuous measurements, data reproducibility was ensured through long-term operational stability of the monitored parameters. The following parameters were measured continuously, 1) current (also current density), 2) applied anode potential, 3) theoretical volume of hydrogen produced, and 4) actual volume of gas produced. The above-mentioned parameters were recorded every 300 s. A confidence interval (CI) of 95 % was chosen to validate results of the above-mentioned parameters. The relative margin of error RME (%) was estimated as follows,

$$\text{RME} = \frac{\text{Margin of error}}{\bar{x}_{\text{parameter}}} \times 100 \quad \text{(v)}$$

where $\bar{x}_{\text{parameter}}$ is the sample mean of any of the above mentioned continuously measured parameters during a particular phase. The margin of error is defined as,

$$\text{Margin of error} = \frac{\sigma}{\sqrt{n}} \times z \quad \text{(vi)}$$

where σ is the standard deviation during a particular phase, n represents number of measurements, and z is 1.96 representing a confidence interval of 95 %.

Under these conditions, RME was found to be less than 5 % for all continuously measured parameters ensuring data reliability.

2.7.2. Analytical samples and discontinuous measurements

Analytical samples for COD, SCFAs and ethanol were measured at least in duplicates. Gas samples and ionic conductivity were also assessed in duplicates. pH, temperature, and dissolved oxygen were measured several times every day.

The coefficient of variation (CV) was calculated accordingly,

$$\text{CV} = \frac{\sigma}{\bar{x}_{\text{parameter}}} \times 100 \quad \text{(vii)}$$

All samples exhibited a CV of less than 5 % indicating acceptable analytical precision.

2.8. Experimental conditions and overview of the RDBER's operation

This work evaluated the performance of the RDBER with respect to key system parameters through parametric analysis, i.e., systematically varying one parameter while keeping others fixed during a 200-day operational period. The analysis of a specific parameter during the course of the experiment is categorized as a phase (see Fig. 2 and Table 1). There are seven phases in total, with phases I to V being operated under sterile conditions, while phases VI and VII were run under unsterile conditions. Under sterile conditions (phases I to V), any liquid-based medium that was introduced, was sterile filtered (0.2 μm) and autoclaved to avoid external contamination. In contrast, the liquid-based mediums introduced in phases VI and VII were not sterilized. A detailed description of the phases can be found in Table 1. In addition, after the 200-day experiment, the RDBER was assessed for limitations and potential improvements by analyzing the biofilm distribution on the anodes.

The phases evaluated are as follows,

1) phase I: start-up,
2) phase II: effect of applied anodic potential before and after dilution with anaerobized sterile demineralized water,
3) phase III: effect of applied anodic potential before and after dilution with sterilized (autoclaved-microfiltered) hydrolyzate,
4) phase IV: impact of disk rotation and recirculation rate,
5) phase V: influence of ionic conductivity,
6) phase VI: continuous feeding of particle-free unsterilized synthetic hydrolyzate, and.
7) phase VII: continuous feeding of unsterilized microfiltered hydrolyzate (not particle-free).

In phase VII, there two sub-phases phases VII (A) and VII (B) (see Table 1 for detailed description).

The system underwent three inoculations, 1) at the beginning of the cultivation with the dual-species (*G. sulfurreducens* and *S. oneidensis*), 2) during the start-up batch (phase I) once the current densities peaked (around day 20), where only *G. sulfurreducens* was reintroduced into the system, and 3) at the end of phase V, with *Desulfuromonas acetexigens*.

3. Results and discussions

3.1. Batch phases I to V with dual species-inoculation in a sterilized liquid medium

3.1.1. Phase I — initial adaptation phase

The applied anode potential ($E_{\text{anode, app}}$) was maintained at 0 mV vs SHE for around 0.3 h, after which it was increased to 300 mV vs SHE. At this time (until 0.3 h), there was notable oxygen production and dissolved oxygen (DO) concentration reached as high as 18.4 mg•L^{-1} (see SI Fig. 3 for DO values) even at 0 mV vs SHE. DO continued to increase to 22.5 mg•L^{-1} for a few minutes, and then stabilized in the range of 19.2 mg•L^{-} for around 15 h. The initial production of oxygen is unclear, and can be attributed to water electrolysis. Thereafter, there was complete depletion of DO after 1.5 d due to oxygen reduction to water at the anode (now cathode), as the polarity is reversed. This was characterized by the negative current densities at the start. After DO depletion current values became less negative from −11.8 mA to −9.4 mA (Fig. 3A). This was followed by a slow increase in current until around day 12 up to around 200 mA.

3.1.2. Phase I — effect of pH

The pH-value, as mentioned earlier, started at 7, but over time decreased to around 6 on day 12. To restore initial conditions, pH-value was increased from 6 to 7.7. This increase coincidentally led to the highest peak in current which stabilized until day 30 (see Fig. 2A). The addition of a highly conductive solution to raise the pH (0.2 L of 2.5 M NaOH) can have two potential effects,

1) an optimum pH for electroactivity of *G. sulfurreducens* within the electroactive biofilm (EAB) since the pH within the EAB is relatively lower in comparison to pH in the bulk solution [32], and.
2) reduced electrolyte resistance and the associated internal resistance [33]. This effect of reduced internal resistance is also further discussed in phase V (influence of ionic conductivity).

During this peak (phase 1) of the highest current, there was a coincidental production of H_2 reaching up to 3.2 L•d^{-1} (equivalent to 36 L•m^{-3}_{reactor} d^{-1}). A steady-state current density of 240 ± 34 mA•m^{-2}_{anode} was achieved in phase I for an 18-day period (Fig. 2B).

To improve upon the current density during phase I, and also since there was considerable concentration of DO in the beginning which could have impeded the growth of these strict anaerobes [34], reinoculation was performed with *G. sulfurreducens*, but this did not have any notable effect on current densities (between days 20 to 30). It is suspected that poor mixing or dead zones in the reactor led to reduced biofilm growth and distribution on the anodes (the reason for limited mixing is further discussed in detail in Section 3.4). Poor mixing limits the nutrient and/or substrate transport, resulting in limitations of turnover rates. This is suspected to be the reason why reinoculation did not show any considerable effect.

3.1.3. Phase I — ethanol as carbon source

Interestingly, during the peak and stabilization in current after the pH increase in phase I, there was a simultaneous consumption of notable concentration of EtOH and HPr, and also the highest production rate of HAc. Following the initial spike of current, further consumption of EtOH but at a relatively lower rate, and the subsequent slow production rates of HAc until the end of phase I was observed (see SI Fig. 4B). This suggests the use of EtOH as a carbon source, however, a direct use of EtOH as a carbon source has not been reported to be a part of the metabolism of *G. sulfurreducens* [35].

However, a significant abundance of homoacetogens (*Sporomusa sphaeroides DSM 2875*) was detected in the planktonic phase, albeit much later, since samples for microbial community analysis were taken between days 97 and 105 and on day 116 (see SI Fig. 7), as well as at the

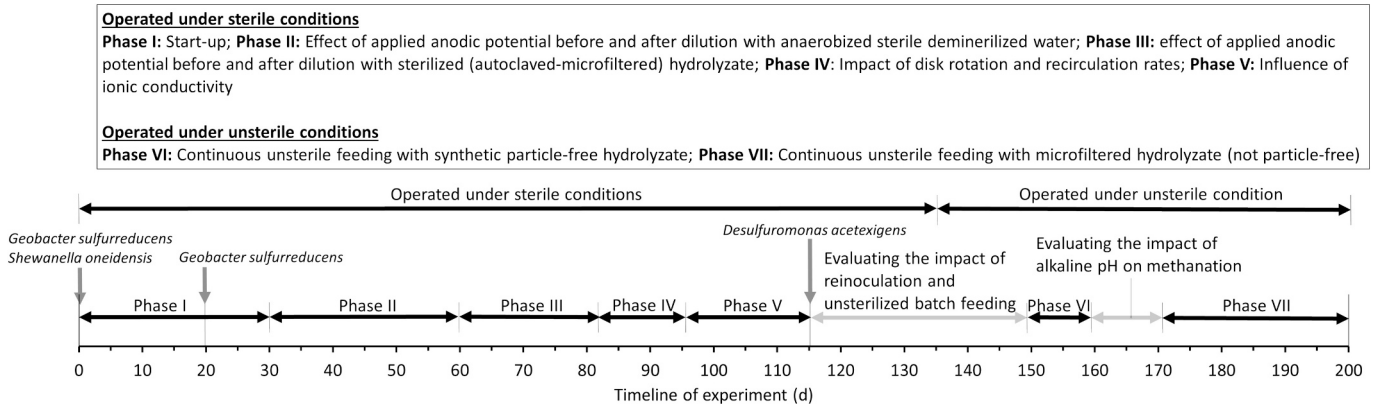

Fig. 2. Timeline of different phases in the RDBER.

end of the experiment (see SI Fig. 8). *S. sphaeroides* were also detected in the cathodic biofilm (after termination of the experiment in which the abundance was 62 %; see SI Fig. 8). The syntrophy existing between *S. sphaeroides* and *G. sulfurreducens* is postulated to have led to the spike in current [36]. A detailed description of the metabolic pathway and the corresponding stoichiometric calculation can be found in SI section 2.3. CE-values calculated based on the syntrophy between the two strains as well as based on sCOD-values aligned well at a little over 70 % (see SI Table 2).

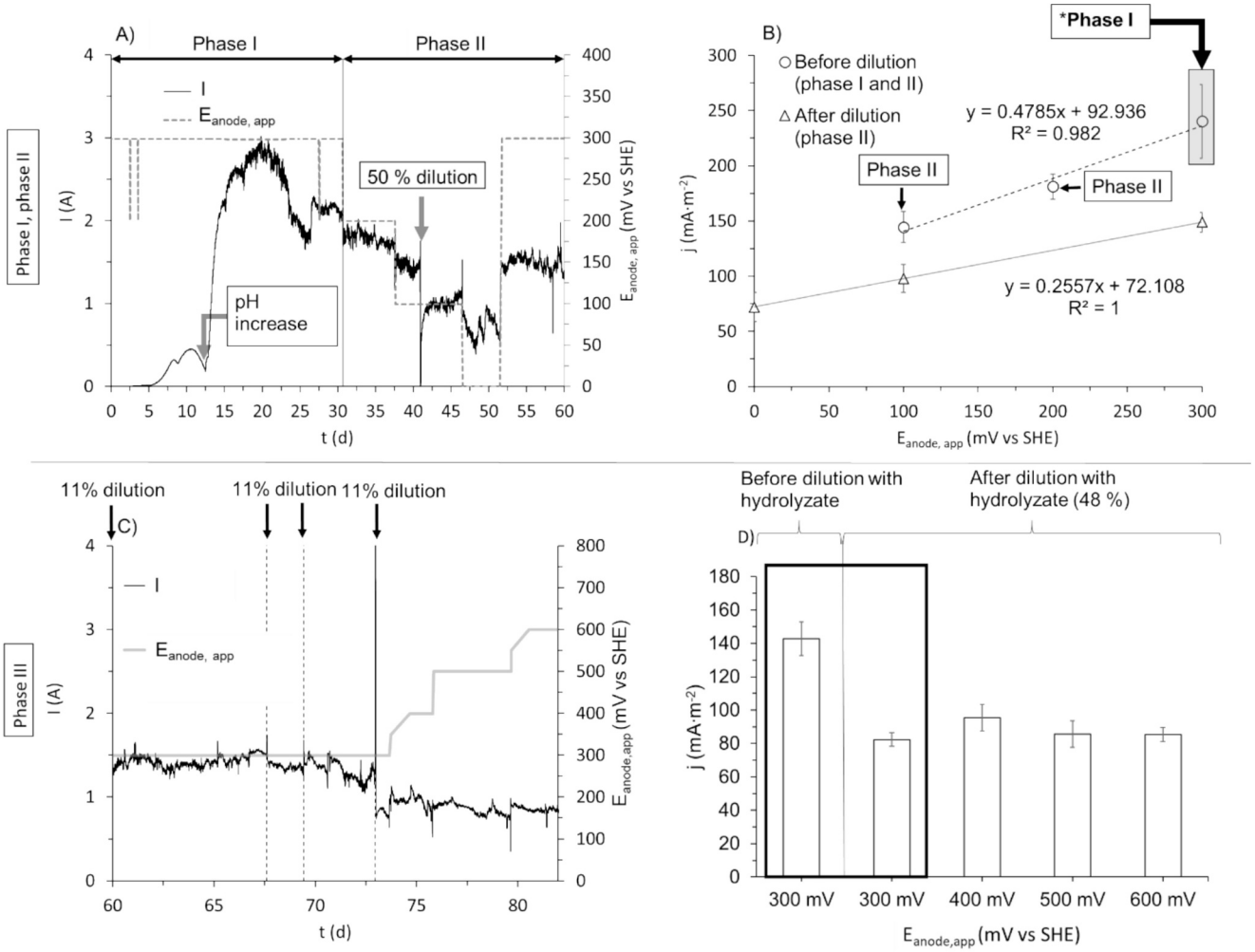

Fig. 3. Start-up phase (phase I) and effect of applied anodic potentials ($E_{anode,\ app}$) before and after dilution (phase II) with anaerobized sterile deionized water on A) current (I) and B) current density (j). Conditions: Anode disk rotation of 1 rpm, temperature of around 30 ± 1 °C, pH 7.3 ± 0.3, and recirculation rate of 0.9 h^{-1}. Note: The shaded rectangle in panel B shows averaged values of steady-state current density in phase I (values were averaged after pH increase until the end of the phase). Effect of applied anodic potentials ($E_{anode,\ app}$) before and after dilution with sterilized (autoclaved-microfiltered) hydrolyzate (phase III) on C) current (I) and D) current density (j) after dilution with hydrolyzate in phase III. Conditions: Anode disk rotation of 1 rpm, temperature of around 30 ± 1 °C, pH 7.3 ± 0.3, and recirculation rate of 0.9 h^{-1}.

3.1.4. Phase II — effect of applied anodic potential before and after dilution with anaerobized sterile demineralized water

In phase II, the batch continued, and in this phase the effect of applied potential at the anode ($E_{anode,\ app}$) was tested to analyze the limiting potential and the subsequent response in current. There are two parts in this phase, one before and one after dilution. Dilution was performed on day 41 as the concentration of HAc reached around 55 mM (see SI Fig. 4B), and along with HPr, SCFAs concentration was at around 65 mM. Härrer et al. [37] studied the synergistic effect of SCFAs mixture, and observed inhibition of *G. sulfurreducens* at concentrations of higher than 50 mM of SCFAs. For this reason, the medium was diluted to approximately 50 % by removing 45 L of the reactor medium while having the outlet of the gastrap connected to an N_2 source and replacing the same volume with anaerobized sterile deionized water to lower the concentration. $E_{anode,\ app}$ was changed before and after dilution between 0 and 300 mV vs SHE (Fig. 3A), and current density was averaged at different $E_{anode,\ app}$.

It can be clearly seen that post dilution, the effect of $E_{anode,\ app}$ showed a relatively smaller slope value (0.26 $mA \bullet m^{-2} \bullet mV^{-1}$) in comparison to the slope of 0.48 $mA \bullet m^{-2} \bullet mV^{-1}$ before dilution (see Fig. 3B). The reason for the reduced slope value after dilution can be attributed to the following, 1) sloughing of certain part of biofilm as the medium was pumped out and/or 2) reduction in the electrolyte conductivity due to dilution, and the corresponding increase in internal resistance. In any case, a significant increase in current density was observed before and after dilution at 300 mV vs SHE. CE-values showed a downward trend before dilution with increasing $E_{anode,\ app}$, and the opposite after dilution (SI Fig. 6 and SI Table 4). Higher CE-values after dilution at 300 mV vs SHE implies a better substrate uptake by the EAB. This could be due to the reduced inhibition as a consequence of lower concentrations of SCFAs mixture as shown by Härrer et al. [37].

3.1.5. Phase III — effect of applied anodic potential before and after dilution with sterilized (autoclaved-microfiltered) hydrolyzate

In phase III, sterilized anaerobized hydrolyzate (see SI Table 1 for composition) was introduced on specific days to monitor the change in current and the response to the hydrolyzate. 11 % of the reactor medium was replaced by sterilized anaerobized hydrolyzate on specific days (60, 68, 69 and 73) and then run as a batch. Following the four hydrolyzate dilutions (48 % dilution in total) a range of applied potentials ($E_{anode,\ app}$) were tested between 300 and 600 mV vs SHE to see whether the positive correlation between potential and achieved current density extends to potentials above 300 mV vs SHE.

Fig. 3C illustrates that the current remains fairly stable until the third dilution. After the fourth dilution, there is a significant reduction by around 43 % in comparison to the starting point. Sloughing off of biofilm is not necessarily a factor here, as there should have been reduction in current after each dilution step. Since the reduction is strongest after the fourth dilution, the effect can be attributed to the hydrolyzate used itself. For the first three dilutions, the composition of the hydrolyzate was rather similar with a higher SCFAs fraction (averaging at 91 % with respect to sCOD), while in the fourth dilution, the ratio of SCFAs (as COD equivalents) to sCOD is only 66 % (see SI Table 1), meaning a large fraction is unclassified dissolved organic carbon that could be presumably not-easily degradable, which could have hindered electroactivity. Looking into the applied potential, the lack of increase in current at higher applied potentials than 400 mV vs SHE is attributed to the oxidative stress on EABs leading to cell impairment and inhibition [38,39]. Also, it can be deduced that the applied potential until 400 mV vs SHE has made the energy barrier low enough for the highest substrate oxidation, and an increase in $E_{anode,\ app}$ above 400 mV vs SHE is not limiting.

3.1.6. Phase IV — impact of disk rotation speed and recirculation rates on hydrodynamics

Maximum value of current achieved until the end of phase III was 3 A, and could not be further improved with reinoculation nor increased potential. Hence, hydrodynamic limitations were suspected to cause insufficient mass transfer in the system and limit the current.

The anodic rotation speed and the medium recirculation rate were incrementally increased. The anode rotation speed was increased in two steps from 1 to 1.2 rpm (day 82) and 1.4 rpm (day 84), however no noticeable impact on current was visible. The lack of increase in system performance at higher rotational speeds can be explained by the arrangement of the anodes. Since the anodes are spaced closely together (at 1.2 cm), there is very low relative velocities between subsequent anode disks, and since there is no significant improvement in relative velocities with increased rotational speed, there is no increase in mass transfer that supports higher electroactivity. The rotational speed was further increased to 2 and 3 rpm between phases V and VI (see Section 3.1.7) with no changes in current production, signifying the role of low relative velocities impeding reactor performance. Similar results were also observed by Xiao et al. [26], where an increase in rotational speed from 1 to 2 rpm showed no improvements in electroactivity. The phenomenon of low relative velocities is further discussed in Section 3.4 where biofilm distribution is analyzed.

In contrast, increasing the recirculation rate stepwise from 0.9 to 3 h^{-1} until day 96 had a pronounced effect on current (see Fig. 4A). The current density could be enhanced by around 100 % (Fig. 4B) in comparison to 0.9 h^{-1}. This increment in current could also be supported by the substrate uptake as evidenced by the higher CE-values (see SI Table 4). With higher recirculation, there is a higher substrate transport to the biofilm as well as improved proton transport from the biofilm into the bulk phase and subsequently to the cathode. This phenomenon also led to a more stable hydrogen production (Table 2). Also, hydrogen recycling occurred in the system. A part of H_2 is redissolved into the system due to the higher recirculation rates, as CE-values were very high, reaching over 200 % (see SI Table 4). Due to pump capacity constraints, it is anticipated that higher flow rates (much more than 3 h^{-1}) could enhance substrate transport and subsequently higher current production, however, this needs to be validated.

3.1.7. Phase V — Influence of ionic conductivity on internal resistance

In phase V, from day 96 to day 110, the influence of ionic conductivity was examined. Conductivity was measured in phase IV, and was found to be 2.6 $mS \bullet cm^{-1}$ (measured on day 90). Between days 96 and 104, the medium in the reactor was spiked twice with a 3.4 M KCl-salt solution to increase the ionic conductivity. Following the second spike, it can be seen that the conductivity reached around 16 $mS \bullet cm^{-1}$. In any event, there was a strong increase in current at both spikes (maximum of 3.5 A and 2.8 A at the first and second spike, respectively), but was followed by a steady decline, and stabilizing to a level that was achieved in phase IV (around 1.6 A) (see Fig. 4C). The average current densities achieved in phase V after the two spikes were more than 230 $mA \bullet m^{-2}$ (see Fig. 4D). The 1.4-fold increase in current densities can be explained by the decreased internal resistances due to the increased electrolyte conductivity (decreased ohmic losses) [40,41]. Although there is a decrease in the internal resistance at the point when the salt solution is added, it is not accompanied by a higher substrate consumption, and hence the current returns to the original state. It can be postulated that along with further enhancement in mass transfer and lowered internal resistance, the system performance could be significantly improved. In general, among the tested parameters in phases I to V, only the recirculation rate showed a very high impact on current production.

3.1.8. Reinoculation with Desulfuromonas acetexigens (between phases V and VI)

The disparity between theoretical hydrogen production and harvested hydrogen yield (Table 2) was suggested to be caused by the reoxidation of hydrogen by *G. sulfurreducens*. To counter hydrogen shuttling and improve hydrogen yield, the RDBER underwent a third

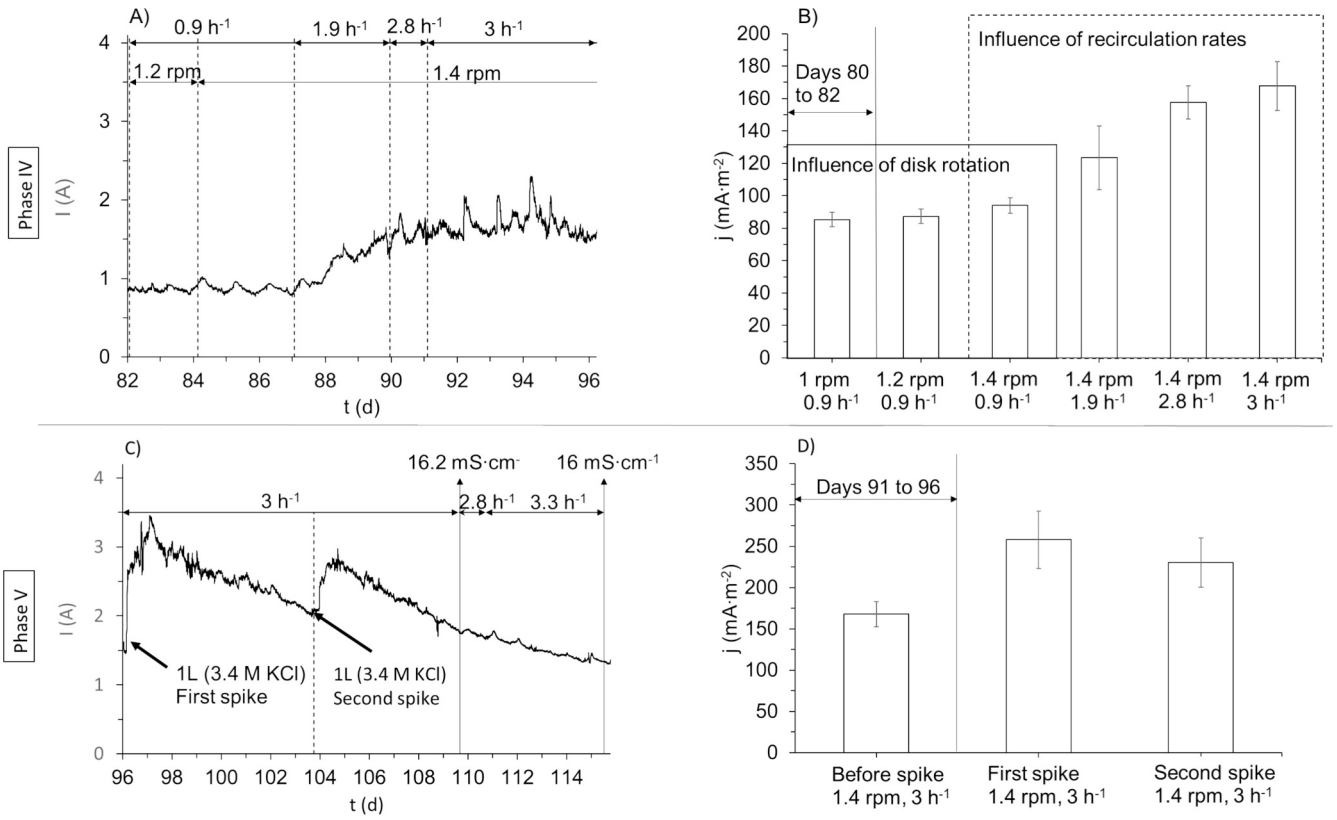

Fig. 4. Impact of disk rotation speed and recirculation rate (i.e., recirculation rate ($m^3 \bullet h^{-1}$)/reactor volume (m^3) or h^{-1}) on hydrodynamics in phase IV on A) current (I) and B) current density (j). Conditions: Temperature of 30 ± 1 °C, pH 7.3 ± 0.3, applied potential = 600 mV vs SHE and recirculation rate of 0.9 h^{-1}. Influence of ionic conductivity on internal resistance in phase V on C) current (I) and D) current density (j). Conditions: Temperature of 30 ± 1 °C, pH 7.3 ± 0.3, applied potential = 600 mV vs SHE.

inoculation on day 115 with *Desulfuromonas acetexigens* (Fig. 5A**)**. Both *G. sulfurreducens* and *D. acetexigens* have been found to be enriched in electroactive biofilms inoculated with sludge and wastewater [42,43]. However, *D. acetexigens* have been shown to produce higher current densities in comparison to its counterpart [44]. Also, *G. sulfurreducens* has the ability to use H_2 as an electron donor [44], and this can have an overall impact on the volumetric yield of hydrogen—a setback that can be avoided with *D. acetexigens* [45].

After inoculation, the system was monitored for changes in current at an $E_{anode,\ app}$ of 600 mV vs SHE for around 6 days. As no notable improvement was observed, $E_{anode,\ app}$ was reduced to 300 mV vs SHE, as it was established earlier that there was no significant difference in current between 300 and 600 mV vs SHE (see Fig. 3D), and also the oxidative stress could be avoided; the rotation of the anode was increased to 3 rpm after a certain period to improve substrate convection, but this showed no notable difference due to low relative velocities (as discussed earlier). Despite a long start-up phase following the second inoculation (around 20 days), there was no significant change in current (Fig. 5A). Interestingly, the microbiome analysis of the anodic biofilm at the end of the experiment and 85 days after inoculation revealed that there was no detectable abundance of *D. acetexigens*, which means that the cells did not become established in the RDBER (see SI Fig. 8).

3.2. Continuous feeding with unsterile hydrolyzate (phases VI and VII)

On days 135 and 136, 10 L of medium in the RDBER was replaced with unsterilized hydrolysate to test for the system's behavior under real conditions. The days that followed the second replacement of the hydrolyzate (on day 136) were monitored in a batch mode. Between days 146 and 149, due to the faster degradation of HAc via methanation, the reactor was spiked twice with sodium acetate (not shown) to avoid complete carbon source depletion before continuous feeding started on day 149. Phase VI and phase VII were operated with synthetic hydrolyzate, and hydrolyzate spiked with SCFAs, respectively (see SI Table 1 for complete composition).

In any case, feeding with a synthetic substrate (phase VI) led to higher current generation (see Fig. 5A) in comparison to phases VII A and VII B, where hydrolyzate was used. One reason would be the low HRT used in phase VI which can lead to an increased washout of methanogens and maintain higher electroactivity. Also, the presence of particles in the hydrolyzate (used for phases VII A and VII B) can adhere to the anodic biofilm and act as an interference by inhibiting substrate diffusion to the anode. Comparing VII A and VII B, it is rather clear that alkaline pH-values can slightly mitigate methanation, but this also has a negative effect on the current. The reduced methanation can be seen from the slightly improved gas quality (Table 2**)** and also the higher CE-values (Fig. 4B). This shows that the electrons produced from sCOD removal were utilized more towards current generation, and less towards methane production. Nevertheless, the sCOD removal was low in general (10 to 20 %) and extremely low in case of VII B (SI Fig. 10).

Interestingly, in phase VI, HAc and HPr were consumed (SI Fig. 10) and there was production of HBu in the effluent, while in phases VII A and B, HAc and HBu were consumed, and HPr was detected in the effluent. It is unclear as to whether there was a shift in the microflora when the hydrolyzate was fed in phases VII A and B. HBu was removed as high as 50 % in phases VII A and B.

In the continuously operated phases, the highest current density was achieved in phase VI (166 ± 42 $mA \bullet m^{-2}$), and this value reduced to 95 ± 28 and 71 ± 18 $mA \bullet m^{-2}$ in phases VII A and B, respectively (Fig. 5B).

Table 2
Theoretical H_2 production ($V_{H2,th}$) based on current values, and average and maximum harvesting rates of H_2 ($V_{H2,harv}$) and CH_4 ($V_{CH4,harv}$), and average gas composition.

Phases	pH	$V_{H2,th}$ ($NL \cdot m_{reactor}^{-3} \cdot d^{-1}$)		$V_{H2,harv}$ ($NL \cdot m_{reactor}^{-3} \cdot d^{-1}$)			$V_{CH4,harv}$ ($NL \cdot m_{reactor}^{-3} \cdot d^{-1}$)			H_2 (%)		CO_2 (%)		CH_4 (%)	
		μ	σ	μ	σ	Max	μ	σ	Max	μ	σ	μ	σ	μ	σ
I	6.9	268	37	3.4	8.7	35.5	ND	ND	ND	87	13	13	13	ND	-
II	7.5 ± 0.1	149	46	0.7	2	9.4	ND	ND	ND	85	5	15	4	ND	-
III	7 ± 0.1	142	32	0.4	1	3.5	ND	ND	ND	78	3	22	3	ND	-
IV	7.3 ± 0.1	144	42	1.6	1.3	3.9	ND	ND	ND	76	-	24	-	ND	-
V	7.5 ± 0.1	287	39	2.7	2.2	6	ND	ND	ND	77	-	23	-	ND	-
VI	8.4 ± 0.3	185	33	3.2	1	4.9	32.8	12.9	50	8	1	4	2	88	2
VII A	7.9 ± 0.1	105	32	0.2	0.2	0.34	2.1	1.4	3.1	8	-	5	-	87	-
VII B	8.6 ± 0.1	87	21	0.6	0.7	1.9	3.8	4.6	12	12	1	4	-	84	1

μ - Average, σ – Standard deviation, ND - Not detected; "-"negligible standard deviation (low coefficient of variation). The double line indicates the phase (VI) in which unsterilized hydrolyzate was fed.

3.3. Gas production and quality

In general, gas production rates were inconsistent during the phases I, II and III. The volume of H_2 that was harvested in comparison to the volume theoretically produced is around 1 %. The low recovery of hydrogen (under sterile conditions) are mainly due to the following reasons, 1) physical retention of hydrogen bubbles, 2) consumption of H_2 by *S. sphaeroides* growing on the cathode, and 3) reoxidation of H_2 by *G. sulfurreducens* [44]. Despite the modified cathodic configuration, there is significant retention of hydrogen bubbles within the system as evidently see in SI Fig. 5. The physical retention or trapping of H_2 bubbles on the cathode facilitates H_2 consumption by *S. sphaeroides* before evolving into the gaseous phase. Reoxidation of H_2 is prevalent as evident from the high CE-values (over 100 %) in the batch phases. In their study on a bench-scale RDBER, Xiao et al. [26] clearly highlighted the reoxidation of H_2 at the cathode with CE-values reaching as high as 353 %. Although it is important to mention that the cathodic configuration was a set of semi-circular cathode disks arranged closely between the anodes as mentioned in Section 2.1. With the modified half-cylindrical cathodic configuration as in this study, the authors observed that reoxidation was still prevalent (CE = 155 %) but lower. In phases IV and V, the higher recirculation rates led to a higher and stable hydrogen production (see Table 2). Other than the higher substrate uptake mentioned before, it is also posited that a higher recirculation rate may have caused some of the trapped H_2-bubbles on the cathode to be sheared off and subsequently be part of the hydrogen loop and reoxidation, as CE-values in phase V reached as high as 397 % (see SI Table 4).

Evaluating the gas composition, it is important to note that a rather high gas purity (Table 2) could be maintained with H_2-fraction averaging at around 80 % during phases I to V. This can be attributed to the careful initial two-step chemical sterilization that was carried out before start-up. The lack of methanation can also be confirmed by the complete absence of methanogenic archaea (in the planktonic phase) based on samples before the unsterilized hydrolyzate was introduced (see SI Fig. 7). During the preceding sterile operational phases, gas fraction of more than 80 %-H_2 could be maintained over 130 days. However, within a few days after the unsterilized hydrolyzate was fed, there was a rise in methane fraction to more than 80 % despite a long and defined dual-species start-up with a sterilized medium. The introduction of real hydrolyzate clearly introduced methanogens in the system, and archaeal analysis at the end of the experiment revealed the presence of methanogens in the anodic biofilm and planktonic phase, though none in the cathodic biofilm (see SI Fig. 9). However, looking into the pattern of methanation, the rise in CH_4 fraction was concomitant with a decrease in H_2 and CO_2 fraction hinting at hydrogenotrophic methanation [46] by supposedly utilizing the redissolved H_2. In contrast, the faster degradation rate of acetate (days 142 and 146 – not shown) indicates the occurrence of acetoclastic methanogenesis.

As mentioned earlier, phases VI and VII were operated in a continuous mode with unsterilized hydrolyzate. Table 2 clearly shows a complete shift in gas fraction towards a mixture of H_2, CH_4 and CO_2 in phases VI and VII when the unsterilized hydrolyzate was fed. The shift in gas composition clearly shows that an MEC (specifically single chamber) implemented at a WWTP should always account for a large CH_4-fraction. Alkaline pH was maintained in phases VI and VII mainly to reduce methanation, as methanogens are more active in a neutral range (pH 6 to 7) [47]. Although methanogens can exhibit considerable activity in the alkaline range used in this study (pH 8 to 8.5) [47], it is also important to maintain electroactivity as extreme pH conditions can be detrimental [48]. Nevertheless, a slight suppression of methanogenesis was observed when pH was increased to around 8.5 in phase VII B (see Table 2). Interestingly, the second RDBER which was operated under unsterile conditions showed no H_2, and the gas fraction comprised only CH_4 and CO_2 (averaging at 80 % to 20 %; see SI Fig. 11). An inference from the comparison of the two RDBERs is the fact that a sterilized start-up phase with defined cultures could maintain a notable concentration of H_2 in the gas phase along with CH_4 (Table 2). Such a gas mixture can be referred to as biohythane, wherein the typical concentration is 5 to 25 % H_2 [49].

3.4. Biomass distribution analysis to evaluate reactor performance

In order to understand the factors limiting the performance of the RDBER, the reactor was dismantled after the 200-day run and evaluated for the distribution of biofilm on the anode disks. The three analysis methods for biofilm characterization are listed below and described in detail in the SI section 1.5:

1) digital photographs to determine effective surface coverage (SC_{eff}) (all disks)
2) OCT images to determine mean biovolume ($\overline{BV}$), and substratum coverage (SC) (selected disks)
3) gravimetric analysis to determine normalized biomass (m_N) (selected disks)

Fig. 6A to D show the difference in biofilm distribution along the reactor length depending on the spatial arrangement of the disks. Disks

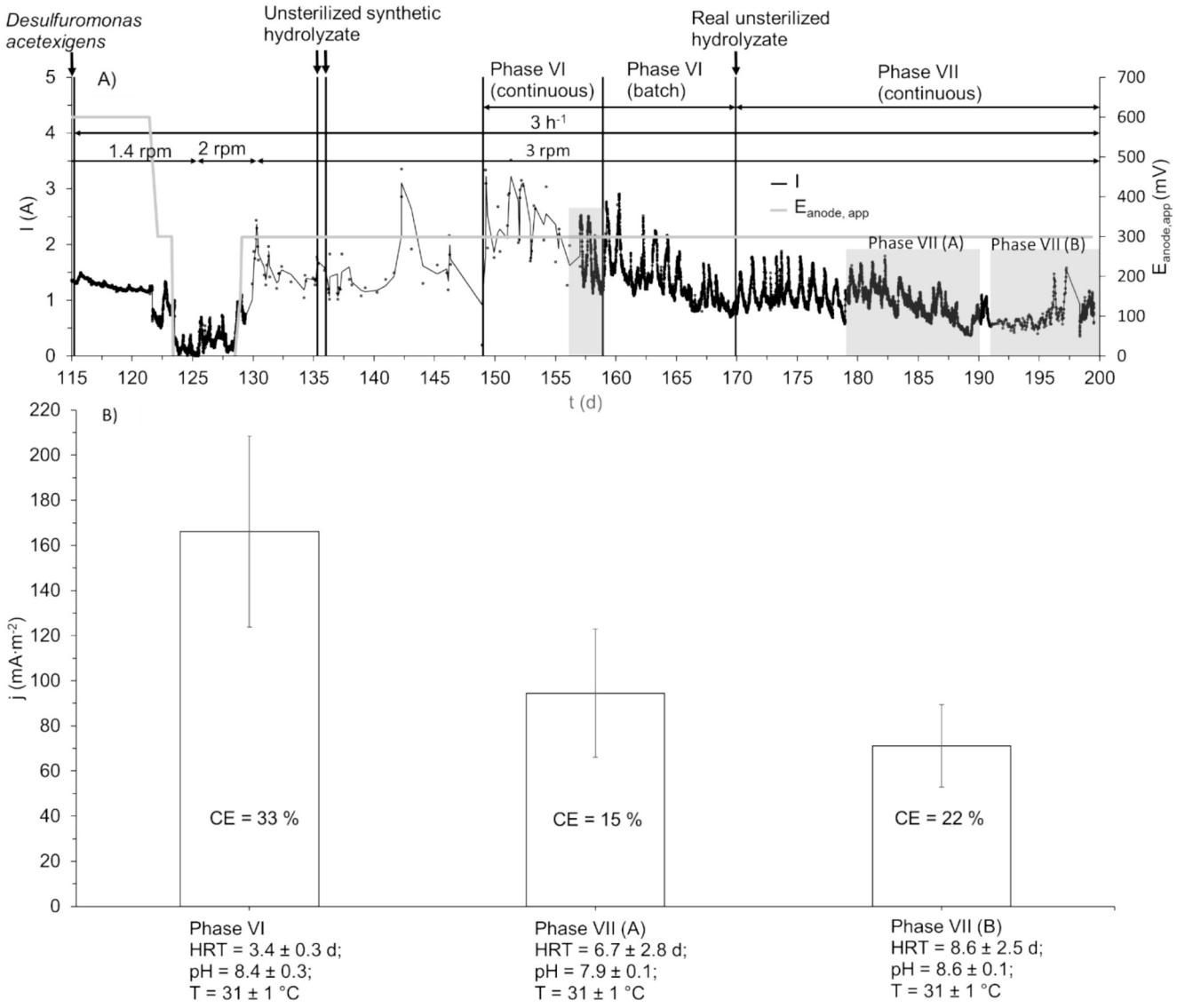

Fig. 5. A) Current (I) and applied potential ($E_{anode,\ app}$), and B) current density (j) for different phases (VI, VII (A) and VII (B)). Conditions: anode rotation = 3 rpm, recirculation rate = 3 h^{-1}. Note: CE = Coulombic efficiency; The coefficient of variation (CV) of current density was 28 ± 1 % for phases VI and VII. The higher CV of current density in these phases is due to notable temperature shifts during the day and night cycle; The grey area in panel A indicates the time range during which liquid samples were taken and the values were averaged for current density (j).

facing the axial direction x represents the leading side of disk and disks facing away from the axial direction x (shown by -x) represents the trailing side side of the disk (see x axis in Fig. 1 for spatial arrangement). Fig. 7A to D depict the distribution along both the reactor length and the radius with respect to both directions.

Examining SC_{eff}, the pattern of distribution is rather similar on both sides. On the anode disks between 50 and 70 cm very little biofilm accumulation was visible. The results of SC_{eff} was corroborated by the normalized biomass (m_N). The lowest values of m_N were seen on the disk at a distance of around 63 cm from the inlet, and m_N was around 0.1 g•m^{-2} and 0.01 g•m^{-2} for x and -x, respectively. Despite relatively scarce data for m_N, correlating m_N and SC_{eff} showed a rather decent fit (see Fig. 6C and D).

Closer inspection of the individual disks for biofilm distribution along the disk radius, led to the observation of an obvious pattern visible from the parameters mean biovolume $\overline{BV}$ and substratum coverage SC obtained from OCT-images. The development of biofilm is more pronounced at a longer radii (see SI Fig. 1C for instance) resembling the shape of an annulus. At radii of 7 and 11 cm along x, average $\overline{BV}$-values are 1.8 ± 2.3 μm^3•μm^{-2} and 3.8 ± 5.8 μm^3•μm^{-2}, respectively, and this parameter is at a similar range along -x, 0.7 ± 0.3 μm^3•μm^{-2} and 1.7 ± 1.9 μm^3•μm^{-2}, respectively. Substratum coverage (SC) shows an obvious pattern as like that as $\overline{BV}$ at 7 and 11 cm along x and -x, averaging at 8 and 27 %, respectively. $\overline{BV}$ and SC are at least 100 % to 200 % higher at a radius of 15 cm in comparison to the lower radius of 11 cm, and it can be as high as 400 % to 1200 % with respect to the lowest radius of 7 cm (see Fig. 7A to D).

Based on these data, there are three major observations, 1) the axial direction, x or -x did not have a notable effect (except for the first and last disk) on the leading or the trailing side of the disks for any of the image-based or gravimetric analysis results (see SI Table 6 and SI Fig. 12 for consolidated results showing the mean values of each parameter for both sides of anode disks), 2) concerning the distribution of biofilm along the reactor length, SC_{eff} was higher and similar in the first half of the reactor, and the last 20 % of the reactor's length, with little to no growth observed between 50 and 70 cm, accounting for around 20 % of the reactor's length and of the anode area, and 3) biofilm growth (based on $\overline{BV}$, SC and the visual observation) was more pronounced along

longer radii until the disks' circumference, thus showed an annular shaped distribution.

The accumulation of an optimal biofilm thickness is a crucial factor affecting electrogenesis in an electroactive biofilm, as a correlation between higher current and biofilm thickness of EABs is shown by several recent publications. For higher current, optimum biofilm thickness is required as overgrown or thicker biofilms can limit electron transfer within the biofilm [50]. Franks et al. [51] reported a biofilm thickness of 50 μm for *G. sulfurreducens* reaching a current density of 3500 mA•m^{-2}, while for the same species, Sun et al. [52] observed a maximum current density of around 4000 mA•m^{-2} at a thickness of 20 μm followed by a reduction until 45 μm. While optimum biofilm thickness is different across several literatures ranging between 20 and 40 μm [50], the observed $\overline{BV}$-values in this study averages at around 5 μm^3•μm^{-2} (mean value of $\overline{BV}$ was 5.0 ± 8.5 μm^3•μm^{-2} (see SI Table 6)) possibly hinting at underdeveloped biofilms on the anode which could explain the relatively low current. More so, *Geobacter* sp. contributed to only around 20 % of the anodic biofilm (see SI Fig. 8).

From these observations, a synergistic effect of both the flow velocity profile and potential distribution is suspected to be a major factor impeding reactor performance by causing low current production. Firstly, evaluating the entire anode stack, the medium convection to inner sections of the reactor is low due to limited recirculation rate which can be seen from the low values of SC_{eff} in Fig. 6A and Fig. 6B. Also, it is important to note that the values of m_N are highest on the first disk along the direction x (leading side) and on the last disk along the direction of -x (trailing side). The higher values could be explained by the presence of a stationary boundary (the reactor itself) and the rotating anode which can potentially improve mass transfer and hence a better biofilm development. Other than the above-mentioned disks, the bulk phase between the anode disks, despite the rotational movement, is susceptible to lower relative fluid velocities between bulk liquid and anode surface, and hence reduced mass transfer due to the small distances between the equally spaced rotating disks. The stagnant bulk phase due to the low relative motion between the anode disks could also explain why an increased rotational speed from 1 to 3 rpm did not have any profound effect, excluding the first and the last disk.

Examining individual anode disks which showed an annular shaped biofilm distribution, the tangential velocity and also the potential distribution are presumable causes for such a specific pattern. Tangential velocity of the rotating disk is a function of radius, and a better substrate uptake occurs along the extended radii favoring more cell attachment and proliferation. However, it is suspected that the tangential velocity predominantly affects the first disk along the direction x (leading side) and on the last disk along the direction of -x (trailing side) due to the stationary boundary formed by the reactor wall. Also, biofilm attachment and development at the outer radius of the disk may have been supported by a lower local internal resistance. The internal resistance (Ohmic loss) increases with distance between anode and cathode, and hence the inner parts of the anode towards the center have a higher local resistance. Therefore, the outer parts or the extended radii of the anode are susceptible to higher current which then decreases towards the center of the anode due to the increased spatial distance from the cathode [53].

3.5. Reactor performance, limitations and improvements

Firstly, considering the results of effective surface coverage (SC_{eff}) of the anode, the question lies in the fact how the RDBER can be improved. It is obvious that mixing and the subsequent hydrodynamics are a limiting factor. A CFD simulation could provide further insight into the velocity profile and flow distribution. Clearly, recirculation rates increased the current density, therefore, a significant increase in recirculation rates is a proposed parameter that requires further

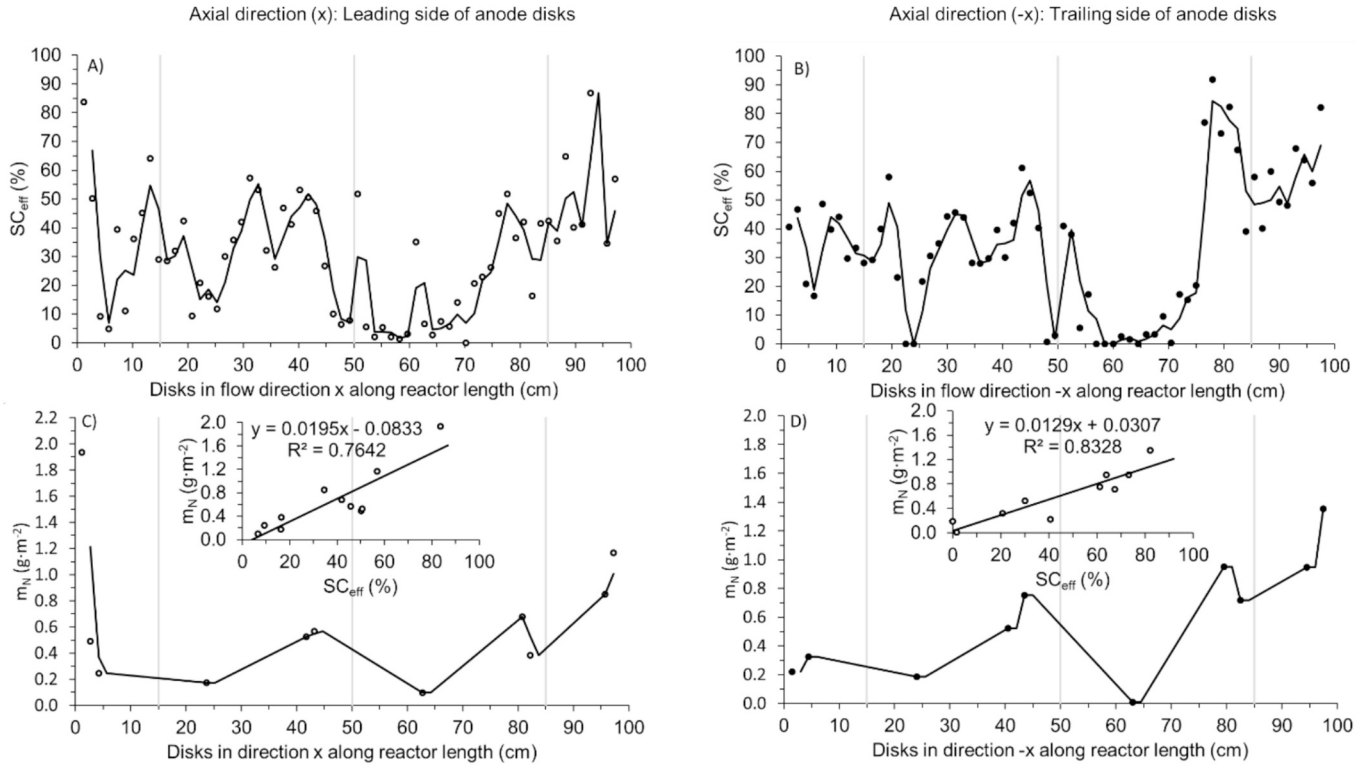

Fig. 6. Effective surface coverage (SC_{eff}) along A) axial direction (x) and B) axial direction (−x). Normalized biomass (m_N) along A) axial direction (x) and B) axial direction (−x). The figures in C and D show the correlation between m_N and SC_{eff}. Note: For disk number 65 (along -x, trailing side), SC_{eff} was calculated based on a relationship between SC_{eff} and the normalized biomass m_N (R^2 = 0.83 m_N = 0.0129•SC + 0.0307; see panels C and D for the relationship between the two parameters). The grey lines in A, B, C and D show the 3 outflow openings at the top of the reactor.

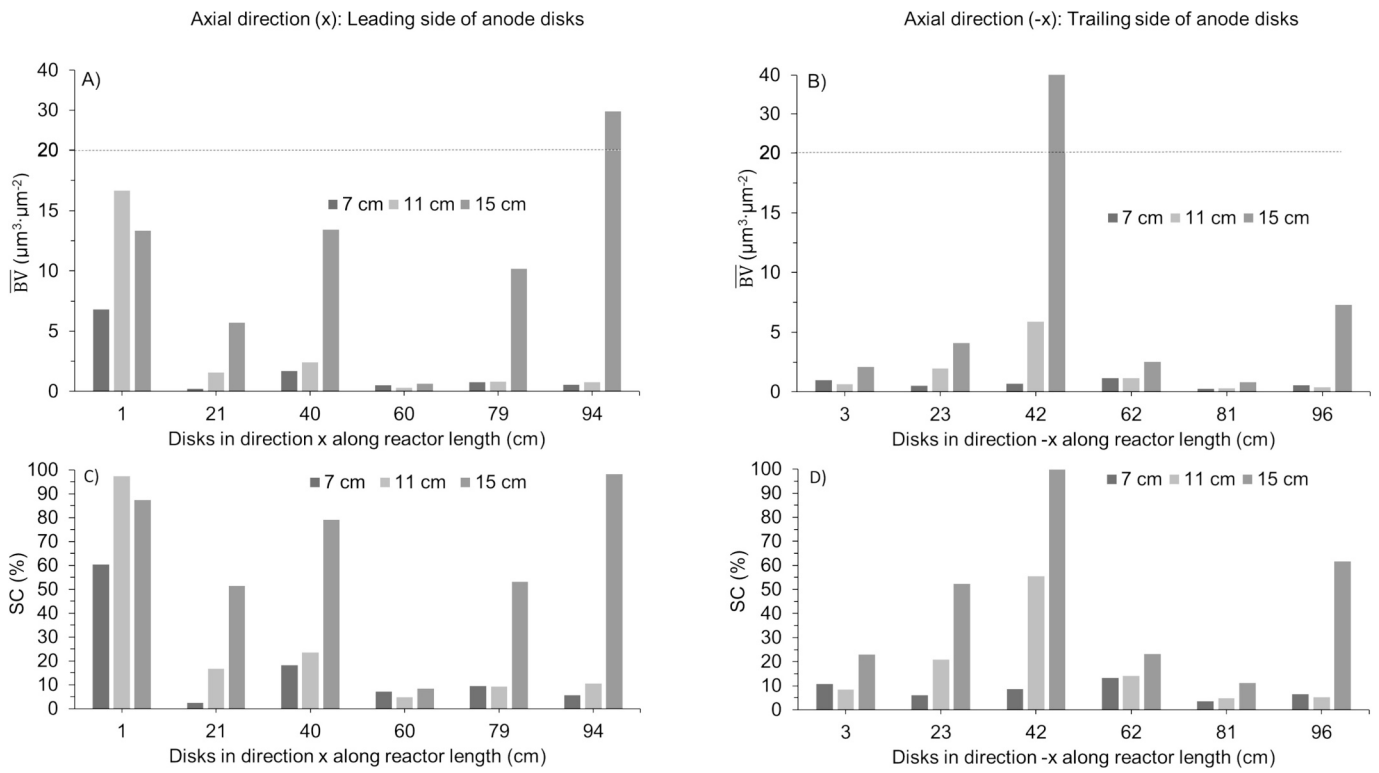

Fig. 7. A) and B) biovolume ($\overline{BV}$)); C) and D) substratum coverage (SC) along the radius for the leading (axial direction: x) and trailing sides (axial direction: -x) of the anode disks.

investigation. In summary, reduced substrate convection and product removal due to low flow velocities in the middle sections of the RDBER is a possible reason that could have affected biofilm distribution.

Nevertheless, the anode area of 10 m^2 is only partially utilized, with the highest value of effective biofilm area (BA_{eff}, see SI equation v for calculation) being only 3.27 m^2. Considering the effective biofilm coverage, current density amounted to 508 ± 128 $mA \bullet m^{-2}_{anode}$. Since the high anode area to reactor volume (100 $m^2_{anode} \bullet m^{-3}_{reactor}$) is one of the underlining features of the RDBER, reducing the number of anode disks may seem contradictory. However, based on the annular shape of the biofilm, a pattern that cannot be necessarily avoided, it would seemingly be more practical to have annular shaped anode disks supported by spokes as the biofilm distribution appears to be governed by the tangential velocity and the potential distribution. Such a design could still maintain a relatively high anode area to reactor volume ratio (approximately 33 $m^2_{anode} \bullet m^{-3}_{reactor}$). Also, having large areas of openings (due to the annular shaped anode disks) along the reactor axis will increase convective transport of the fluid, and the subsequent nutrient and substrate transfer to formerly inaccessible areas of the reactor as well as improved product removal. This value of 33 $m^2_{anode} \bullet m^{-3}_{reactor}$ is still comparatively high and to the best of our knowledge, the highest ratio realized so far at pilot-scale (reactor volume = 175 L) for a MEC was 34 $m^2_{anode} \bullet m^{-3}_{reactor}$ [16].

Secondly, regarding the cathodic recovery, the amount of H_2 harvested is low as seen from the experiments. The RDBER that was operated at bench scale (10 L) had a different cathodic configuration [24]. The cathode was a set of semi-circular disks that were arranged between the circular anode disks close to the lower half. It was posited that such a design would result in significant H_2 consumption as the hydrogen that evolved at the cathode would have to bubble over the anode, where potential H_2 scavengers or even *G. sulfurreducens* itself could utilize H_2 as an electron donor. Although the half cylindrical perforated cathode used here was supposedly an upgraded design to enhance H_2 recovery, the contradictory observed here through low recoveries, possibly indicates that the shear forces created during the anodic rotation in the bench-scale reactor may have aided better H_2 recovery. Utilizing a similar configuration as the bench-scale reactor but with the semi-circular cathode disks close to the upper half of the anode disks is hypothesized to improve H_2 recovery and reduce H_2 scavenging. In addition, the cathode would act as stationary boundary between successive anode disks, potentially improving relative velocities with increased rotational speeds.

At any rate, the RDBER has to be compared with existing MEC reactors for posterity. Phase VI in this study is chosen for comparison with the surveyed pilot-scale MEC reactors in the hundred-liter range (Table 3). The 100-L RDBER is also compared with the 10-L RDBER [24] operated with the defined dual-species start-up conditions to assess the impact of upscaling (see Table 3). A second 100-L RDBER operated for a long-term period only under unsterile conditions at a wastewater treatment plant (see SI section 2.12 for results) was also comapred. It appears that a sterile start-up phase can prevent complete dominance of methanation, as H_2 production (along with CH_4) can still be maintained to a certain extent along with higher current densities and CE-values. The production of biohythane from the RDBER, as mentioned earlier, hints at the opportunity to valorize this gas mixture into an enhanced combustible source for higher energy recovery in comparison to the typical biomethane obtained via anaerobic digestion [54].

At any rate, the volume of H_2 harvested is in the range of some pilot-scale MECs while relatively lower in comparison to others (compare values in Table 3). Although, it is evident that the RDBER can compete in terms of current production, the disadvantage is mainly in the volume of hydrogen that could be harvested. The comparison clearly shows that double chamber MECs perform better when it comes to harvesting hydrogen. This is also evident from the composition of the gaseous, where double chamber MECs have a hydrogen purity of 60 to 100 % in most cases. Despite the sterile start-up phase, the achievable hydrogen quality is around 8 %, clearly indicating that methanogenesis is an inherent problem in single chamber MECs.

Table 3
Literature comparison of pilot-scale MEC reactors. **Note:** AA = Anode area, Conti. = Continuous, RV = Reactor volume, SA_{tot} = Specific anode area (based on total reactor volume), SA_{WV} = Specific anode area (based on working volume), WV = Working volume, WW = Wastewater.

RV/ WV (L)	AA (m^2)	SA_{tot}/SA_{WV} ($m^2_{anode}•m^{-3}_{reactor}$)	Design	Substrate	Mode	pH	T (°C)	HRT (d)	Voltage (mV)	Average stable current density ($mA•m^{-2}_{anode}$)	Average stable current density ($mA•m^{-3}_{reactor}$)	Average theoretical hydrogen ($L\ H_2•m^{-3}_{reactor}•d^{-1}$)	Average harvested hydrogen ($L\ H_2•m^{-3}_{reactor}•d^{-1}$)	CE (%)	Average methane harvested ($L\ CH_4•m^{-3}_{reactor}•d^{-1}$)	Gas fraction	Ref
NR/ 130	1.63	NR / 12.6	Double chamber (cassette type)	Urban WW	Conti.	6 to 7.5	18 to 22	1	1500	250	3100	31	31	82 (maximum)	minimal	95 % H_2	[15]
182/ 175	6	33 / 34	Double chamber (cassette type)	Domestic WW	Conti.	7 to 8.5	8 to 16	0.2	900	294 ± 185	10,000 ± 6000	101	3	10 to 30[b]	ND	60 to 93 % H_2	[16]
135/ 26	0.31	2.3 / 12	Double chamber (cassette type)	Domestic WW	Conti.	8.0 ± 0.3	16 ± 3	1	900 to 1200	160	1900	19	20	NR	NR	98 % H_2	[17]
1000/910	NR	NR	Single chamber (several modules)	Winery WW	Conti.	6.4 ± 0.3	31 ± 1	1	900	NR	6000 to 8000[b]	60 to 80	ND	NR	150 to 250	85 % CH_4	[14]
220/ 135	1.47	6.7 / 10.9	Double chamber (cassette type)	Synthetic WW	Conti.	6.9 ± 0.1	18	2.7	900	1230 (maximum)	13,400 (maximum)	133 (maximum)	99	27	NR	90 % H_2	[8]
220/ 150	1.14	5.2 / 7.6	Double chamber (cassette type)	Industrial WW	Conti.	7	NR	2.5	1300	1000 to 2000	6700 to 15,200	76 to 152	60 to 150 (210 (maximum))	20	NR	NR	[18]
120/ 88	1.96	16.4 / 22.3	Double chamber (cassette type)	Domestic WW	Conti.	6 to 7	17 ± 1	1	1100	270	6000	60	15	55	minimal	100 % H_2 (< 2 % CH_4)	[19]
120/ 88	1.96	16.4 / 22.3	Double chamber (cassette type)	Domestic WW	Conti.	6.7 to 7	12.5	1	1100	NR	340	NR	7	41	ND	100 % H_2	[20]
NR/ 150	2.35	NR / 15.7	Double chamber	WW	Conti.	7.8 ± 0.3	20	1	1000	220	3400	35	NR	3 to 10 %	NR	0 to 10 % H_2	[21]
10/ 10	1	100 / 100	Single chamber (RDBER)	20 mM HAc, 20 mM HLa	Batch[S]	7.4	30	–	0[d]	800 to 1300[c]	80,000 to 1,30,000	800 to 1300	430	NR	ND	88 % H_2	[24]
100/ 90	10	100 / 111	Single chamber (RDBER)	25 mM HAc, 25 mM HLa, 176 mM etOH	Batch[S] (phase I)	7.2 ± 0.2	29	–	300[d]	240 ± 34	27,000 ± 4000	268 ± 37	3.4 ± 8.7 (average) 36 (maximum)	74	ND	87 % H_2	
100/ 90	10	100 / 111	Single chamber (RDBER)	Synthetic hydrolyzate	Conti. (phase VI)	8.4 ± 0.3	31 ± 1	3.4 ± 0.3	300[d]	166 ± 42	18,000 ± 5000	185 ± 33	3.2 ± 1	33	33 ± 13	8 % H_2/ 88 % CH_4	
100/ 90	3.27[e]	100 / 36	Single chamber (RDBER)	Synthetic hydrolyzate	Conti. (phase VI)	8.4 ± 0.3	31 ± 1	3.4 ± 0.3	300[d]	508 ± 128[a]	18,000 ± 5000	185 ± 33	3.2 ± 1	33	33 ± 13	8 % H_2/ 88 % CH_4	This study
100/ 90	10	100 / 111	Single chamber (RDBER)	25 mM HAc, 25 mM HLa	Batch[W]	7.1 ± 0.2	29 ± 4	–	0[d]	30 ± 8	3000 ± 1000	33 ± 9	ND	6	6	85 % CH_4	
100/ 90	10	100 / 111	Single chamber (RDBER)	Hydrol-yzate	Batch[W]	7.1 ± 0.2	29 ± 4	–	0[d]	19 ± 12	2000 ± 1000	21 ± 13	ND	1	40	75 % CH_4	

[a] calculated based on effective biofilm-covered area (BA_{eff}), [b] the values are approximate (**Note**: 7200 $mA•m^{-3}_{reactor}$ was the peak value reported), [c] approximate values (1300 $mA•m^{-2}_{anode}$ is the highest recorded value), [d]applied anode potential vs. SHE, [e] effective area. NR- not reported, ND – Not detected, [W] RDBER operated on-site at a wastewater treatment plant, [S] RDBER operated under sterile conditions. Conti. stands for continuous.

However, it is absolutely essential to consider scalability, as the cassette-type configuration is a numbering-up strategy and could have disadvantages mainly from an economic standpoint. Moreover, Coulombic efficiency (laboratory-controlled RDBER) is 33 %, which is in the range of double chamber MECs. Indeed, there is optimization potential, concerning higher rates of harvesting hydrogen. With further upgrades to reactor architecture, there is great prospect for the RDBER in advancing single chamber MEC technology.

4. Conclusion

In this study, the 100-L RDBER was evaluated as a terminal treatment step for hydrogen production in a wastewater biorefinery. The following conclusions can be drawn,

1) Firstly, the RDBER was operated in a batch mode with the defined dual-species inocula, and several system parameters were optimized. In the start-up phase, current densities stabilized around 240 $mA \bullet m^{-2}$ with a CE in the range of 70 %. Also, during the start-up, the highest volume of hydrogen was harvested, amounting to 36 L $H_2 \bullet m^{-3}_{reactor} \bullet d^{-1}$. Among the tested operational parameters during the batch phase, increasing the liquid recirculation rate threefolds led to a 100 % increase in current production. Operating the batch phase with a sterile medium for a 130-day period prevented methanogenesis, with H_2-fraction averaging at approximately 80 %.
2) After the batch phase, the RDBER was operated in a continuous mode with unsterile hydrolyzate. Results show that feeding the reactor with a particle-free hydrolyzate at a low HRT (around 3 days) improved the RDBER's performance. Current density amounted to 170 $mA \bullet m^{-2}_{anode}$ with an average CE of 33 %. While feeding unsterile hydrolyzate, methanation was dominant, and a gas mixture comprising of hydrogen and methane (biohythane) was obtained (9 % H_2:86 % CH_4). The average yield of H_2 and CH_4 in the continuous phase was 3 L $H_2 \bullet m^{-3}_{reactor} \bullet d^{-1}$ and 33 L $CH_4 \bullet m^{-3}_{reactor} \bullet d^{-1}$, respectively.
3) Following the operation of the RDBER, the reactor was dismantled to analyze biofilm distribution. Image and gravimetric analyses showed an incomplete biofilm distribution along the reactor length and along the anodes' radii. The substrate transport to the inner sections of the reactor as well as along the span of the anode disks is low due to the close arrangement of the anode disks and the limited recirculation. Also, OCT images revealed an annular-shaped biofilm coverage on the anode disks. The reason was attributed to the tangential velocity and the potential distribution profile on the anodes. Based on the results of surface coverage, only one-third of the total anode was covered. Current density with respect to the effectively covered area was around 510 $mA \bullet m^{-2}_{anode}$.

The RDBER is still an attractive design within the class of single-chamber bioelectrochemical systems, especially due to its high specific anode area. The values of current density and hydrogen production still need to be improved to merit a full-scale implementation in a biorefinery. Based on the results of biofilm distribution, the performance of the RDBER can be improved with an upgrade in electrode configuration and reactor medium mixing.

CRediT authorship contribution statement

Nikhil Shylaja Prakash: Writing – original draft, Methodology, Investigation, Data curation, Conceptualization. **Willow Neske:** Writing – review & editing, Methodology, Investigation, Data curation, Conceptualization. **Max Rümenapf:** Writing – review & editing, Methodology, Conceptualization. **Zhizhao Xiao:** Writing – review & editing, Methodology, Conceptualization. **Andreas Netsch:** Writing – review & editing, Methodology, Conceptualization. **Harald Horn:** Writing – review & editing, Supervision, Funding acquisition. **Jonas Ullmann:** Methodology, Conceptualization. **Johannes Eberhard Reiner:** Methodology, Conceptualization. **Andrea Hille-Reichel:** Writing – review & editing, Validation, Supervision, Funding acquisition, Conceptualization.

Funding

Finally, the authors would like to express their thanks to the Baden-Württemberg Ministry for the Environment, Climate and Energy Management and the European Union (EU) for funding the project KoalA-plan (https://www.umwelttechnik-bw.de/en/node/508).

Declaration of competing interest

The authors declare that they have no known competing financial interests or personal relationships that could have appeared to influence the work reported in this paper.

Acknowledgements

First and foremost, we dedicate this publication to Max Hackbarth, the inventor and designer of the bioelectrochemical prototype reactor presented in this paper. Max Hackbarth deceased in November 2024, prior to the submission of this article. With his passing, we have not only lost a brilliant engineer but also a wonderful human being, a trusted colleague, and a cherished friend. We will hold his memory close to our hearts and honor his legacy. The authors would like to thank the colleagues of the mechanical workshop of the Engler-Bunte-Institut, namely Alfred Herbst, Erwin Wachter and Dennis Happle for building the RDBER. Axel Heidt, Ulrich Reichert, and Matthias Weber of Engler-Bunte-Institut, and the technicians of LFL and LFKW, Stuttgart are acknowledged for their assistance in laboratory experiments and analyses. In addition, the authors would like to thank research assistants, Sanchi Rithe, Kenneth Lawrence d'Souza and Thomas Dharmasaputra, for their support in carrying out the experiment. Willow Neske's contribution to this paper was supported through a Fulbright grant of the German-American Fulbright Commission.

Appendix A. Supplementary data

Supplementary data to this article can be found online at https://doi.org/10.1016/j.cej.2025.168691.

Data availability

Data will be made available on request.

References

[1] M. Kitching, R. Butler, E. Marsili, Microbial bioelectrosynthesis of hydrogen: Current challenges and scale-up, Enzyme Microb. Technol. 96 (2017) 1–13, https://doi.org/10.1016/j.enzmictec.2016.09.002.
[2] Y.M. Wong, T.Y. Wu, J.C. Juan, A review of sustainable hydrogen production using seed sludge via dark fermentation, Renew. Sustain. Energy Rev. 34 (2014) 471–482, https://doi.org/10.1016/j.rser.2014.03.008.
[3] W. Liu, et al., Hydrogen generation in microbial electrolysis cell feeding with fermentation liquid of waste activated sludge, Int. J. Hydrogen Energy 37 (18) (2012), https://doi.org/10.1016/j.ijhydene.2012.04.090.
[4] L. Lu, D. Xing, B. Liu, N. Ren, Enhanced hydrogen production from waste activated sludge by cascade utilization of organic matter in microbial electrolysis cells, Water Res. 46 (4) (2012) 1015–1026, https://doi.org/10.1016/j.watres.2011.11.073.
[5] I. Rivera, G. Buitrón, P. Bakonyi, N. Nemestóthy, K. Bélafi-Bakó, Hydrogen production in a microbial electrolysis cell fed with a dark fermentation effluent, J. Appl. Electrochem. 45 (11) (2015) 1223–1229, https://doi.org/10.1007/s10800-015-0864-6.
[6] S. Anantharaj, et al., Membrane free water electrolysis under 1.23 V with Ni3Se4/Ni anode in alkali and Pt cathode in acid, Appl. Surf. Sci. 478 (2019) 784–792, https://doi.org/10.1016/j.apsusc.2019.01.231.
[7] H. Gunaseelan, A.V. Munde, R. Patel, B.R. Sathe, Metal-organic framework derived carbon-based electrocatalysis for hydrogen evolution reactions: A review, Mater Today Sustain 22 (2023) 100371, https://doi.org/10.1016/j.mtsust.2023.100371.

[8] O. Guerrero-Sodric, J.A. Baeza, A. Guisasola, Exploring key operational factors for improving hydrogen production in a pilot-scale microbial electrolysis cell treating urban wastewater, Chem. Eng. J. 469 (2023) 144001, https://doi.org/10.1016/j.cej.2023.144001.

[9] D. Call, B.E. Logan, Hydrogen Production in a Single Chamber Microbial Electrolysis Cell Lacking a Membrane, Environ. Sci. Technol. 42 (9) (2008) 3401–3406, https://doi.org/10.1021/es8001822.

[10] H. Wang, et al., Explore the difference between the single-chamber and dual-chamber microbial electrosynthesis for biogas production performance, Bioelectrochemistry 138 (2021) 107726, https://doi.org/10.1016/j.bioelechem.2020.107726.

[11] B.E. Logan, Scaling up microbial fuel cells and other bioelectrochemical systems, Appl. Microbiol. Biotechnol. 85 (6) (2010) 1665–1671, https://doi.org/10.1007/s00253-009-2378-9.

[12] P. Von Tettau, P. Thiele, P. Mauermann, M. Wick, S. Tinz, S. Pischinger, Per- and polyfluoroalkyl substances in proton exchange membrane fuel cells — a review, J. Power Sources 630 (2025) 236104, https://doi.org/10.1016/j.jpowsour.2024.236104.

[13] K. Sasaki, M. Morita, D. Sasaki, N. Matsumoto, N. Ohmura, Y. Igarashi, Single-chamber bioelectrochemical hydrogen fermentation from garbage slurry, Biochem. Eng. J. 68 (2012) 104–108, https://doi.org/10.1016/j.bej.2012.07.014.

[14] R.D. Cusick, et al., Performance of a pilot-scale continuous flow microbial electrolysis cell fed winery wastewater, Appl. Microbiol. Biotechnol. 89 (6) (2011) 2053–2063, https://doi.org/10.1007/s00253-011-3130-9.

[15] J.A. Baeza, À. Martínez-Miró, J. Guerrero, Y. Ruiz, A. Guisasola, Bioelectrochemical hydrogen production from urban wastewater on a pilot scale, J. Power Sources 356 (2017) 500–509, https://doi.org/10.1016/j.jpowsour.2017.02.087.

[16] S.E. Cotterill, J. Dolfing, C. Jones, T.P. Curtis, E.S. Heidrich, Low temperature domestic wastewater treatment in a microbial electrolysis cell with 1 m^2 anodes: towards system scale-up, Fuel Cells 17 (5) (2017) 584–592, https://doi.org/10.1002/fuce.201700034.

[17] S.E. Cotterill, J. Dolfing, T.P. Curtis, E.S. Heidrich, Community assembly in wastewater-fed pilot-scale microbial electrolysis cells, Front. Energy Res. 6 (2018) 98, https://doi.org/10.3389/fenrg.2018.00098.

[18] O. Guerrero-Sodric, J.A. Baeza, A. Guisasola, Enhancing bioelectrochemical hydrogen production from industrial wastewater using Ni-foam cathodes in a microbial electrolysis cell pilot plant, Water Res. 256 (2024) 121616, https://doi.org/10.1016/j.watres.2024.121616.

[19] E.S. Heidrich, J. Dolfing, K. Scott, S.R. Edwards, C. Jones, T.P. Curtis, Production of hydrogen from domestic wastewater in a pilot-scale microbial electrolysis cell, Appl. Microbiol. Biotechnol. 97 (15) (2013) 6979–6989, https://doi.org/10.1007/s00253-012-4456-7.

[20] E.S. Heidrich, S.R. Edwards, J. Dolfing, S.E. Cotterill, T.P. Curtis, Performance of a pilot scale microbial electrolysis cell fed on domestic wastewater at ambient temperatures for a 12 month period, Bioresour. Technol. 173 (2014) 87–95, https://doi.org/10.1016/j.biortech.2014.09.083.

[21] M. Isabel San-Martín, R. Mateos, B. Carracedo, A. Escapa, A. Morán, Pilot-scale bioelectrochemical system for simultaneous nitrogen and carbon removal in urban wastewater treatment plants, J. Biosci. Bioeng. 126 (6) (2018) 758–763, https://doi.org/10.1016/j.jbiosc.2018.06.008.

[22] J. Sim, R. Reid, A. Hussain, J. An, H.-S. Lee, Hydrogen peroxide production in a pilot-scale microbial electrolysis cell, Biotechnol. Rep. 19 (2018) e00276, https://doi.org/10.1016/j.btre.2018.e00276.

[23] J.J. Fornero, M. Rosenbaum, L.T. Angenent, Electric power generation from municipal, food, and animal wastewaters using microbial fuel cells, Electroanalysis 22 (7–8) (2010) 832–843, https://doi.org/10.1002/elan.200980011.

[24] M. Hackbarth, J. Gescher, H. Horn, J.E. Reiner, A scalable, rotating disc bioelectrochemical reactor (RDBER) suitable for the cultivation of both cathodic and anodic biofilms, Bioresour. Technol. Rep. 21 (2023) 101357, https://doi.org/10.1016/j.biteb.2023.101357.

[25] F. Hassard, J. Biddle, E. Cartmell, B. Jefferson, S. Tyrrel, T. Stephenson, Rotating biological contactors for wastewater treatment – A review, Process. Saf. Environ. Prot. 94 (2015) 285–306, https://doi.org/10.1016/j.psep.2014.07.003.

[26] Z. Xiao, M. Ruemenapf, M. Hackbarth, H. Horn, A. Hille-Reichel, J.E. Reiner, Impact of rotational speed and different counter electrode configurations on bioelectrochemical hydrogen production in a 10 L RDBER, Bioresour. Technol. Rep. 31 (2025), https://doi.org/10.1016/j.biteb.2025.102208.

[27] N. Shylaja Prakash, P. Maurer, H. Horn, F. Saravia, A. Hille-Reichel, Separation of short-chain fatty acids from primary sludge into a particle-free permeate by coupling chamber filter-press and cross-flow microfiltration: optimization, semi-continuous operation, and evaluation, Membranes 15 (1) (2025) 22, https://doi.org/10.3390/membranes15010022.

[28] K. Venkateswaran, et al., Polyphasic taxonomy of the genus Shewanella and description of Shewanella oneidensis sp. now, Int. J. Syst. Bacteriol. 49 (1999) 705–724.

[29] F. Caccavo, D.J. Lonergan, D.R. Lovley, M. Davis, J.F. Stolz, M.J. McInerney, Geobacter sulfurreducens sp. nov., a hydrogen- and acetate-oxidizing dissimilatory metal-reducing microorganism, Appl. Environ. Microbiol. 60 (10) (1994) 3752–3759, https://doi.org/10.1128/aem.60.10.3752-3759.1994.

[30] J.R. Weiler, N. Jürgensen, M. Cornejo Infante, M.T. Knoll, J. Gescher, Strain and model development for auto- and heterotrophic 2,3-butanediol production using *Cupriavidus necator* H16, Biotechnol. Biofuels Bioprod. 17 (1) (2024) 108, https://doi.org/10.1186/s13068-024-02549-7.

[31] M. Wagner, H. Horn, Optical coherence tomography in biofilm research: a comprehensive review, Biotechnol. Bioeng. 114 (7) (2017) 1386–1402, https://doi.org/10.1002/bit.26283.

[32] S.A. Patil, et al., Electroactive mixed culture derived biofilms in microbial bioelectrochemical systems: The role of pH on biofilm formation, performance and composition, Bioresour. Technol. 102 (20) (2011) 9683–9690, https://doi.org/10.1016/j.biortech.2011.07.087.

[33] M.D. Merrill, B.E. Logan, Electrolyte effects on hydrogen evolution and solution resistance in microbial electrolysis cells, J. Power Sources 191 (2) (2009) 203–208, https://doi.org/10.1016/j.jpowsour.2009.02.077.

[34] W.C. Lin, M.V. Coppi, D.R. Lovley, *Geobacter sulfurreducens* Can Grow with Oxygen as a Terminal Electron Acceptor, Appl. Environ. Microbiol. 70 (4) (2004) 2525–2528, https://doi.org/10.1128/AEM.70.4.2525-2528.2004.

[35] S. Viulu, K. Nakamura, A. Kojima, Y. Yoshiyasu, S. Saitou, K. Takamizawa, Geobacter sulfurreducens subsp. ethanolicus, subsp. nov., an ethanol-utilizing dissimilatory Fe(III)-reducing bacterium from a lotus field, J. Gen. Appl. Microbiol. 59 (5) (2013) 325–334, https://doi.org/10.2323/jgam.59.325.

[36] M. Rümenapf, Implementierung des elektroaktiven Deltaproteobakteriums *Desulfuromonas acetexigens* in mikrobiellen Elektrolysezellen, Karlsruher Institut für Technologie (KIT), 2024 [Online]. Available: DOI: 10.5445/IR/1000178701.

[37] D. Härrer, A. Elreedy, R. Ali, A. Hille-Reichel, J. Gescher, Probing the robustness of Geobacter sulfurreducens against fermentation hydrolysate for uses in bioelectrochemical systems, Bioresour. Technol. 369 (2023) 128363, https://doi.org/10.1016/j.biortech.2022.128363.

[38] A. Ding, Y. Yang, G. Sun, D. Wu, Impact of applied voltage on methane generation and microbial activities in an anaerobic microbial electrolysis cell (MEC), Chem. Eng. J. 283 (2016) 260–265, https://doi.org/10.1016/j.cej.2015.07.054.

[39] F. Ndayisenga, Z. Yu, B. Wang, D. Zhou, Effects of the applied voltage on electroactive microbial biofilm viability and hydrogen production in a recalcitrant organic waste-fed single-chamber membrane-free microbial electrolysis cell performance, Chem. Eng. J. 469 (2023) 144002, https://doi.org/10.1016/j.cej.2023.144002.

[40] J.-Y. Nam, H.-W. Kim, K.-H. Lim, H.-S. Shin, B.E. Logan, Variation of power generation at different buffer types and conductivities in single chamber microbial fuel cells, Biosens. Bioelectron. 25 (5) (2010) 1155–1159, https://doi.org/10.1016/j.bios.2009.10.005.

[41] R. Rousseau, S.F. Ketep, L. Etcheverry, M.-L. Délia, A. Bergel, Microbial electrolysis cell (MEC): a step ahead towards hydrogen-evolving cathode operated at high current density, Bioresour. Technol. Rep. 9 (2020) 100399, https://doi.org/10.1016/j.biteb.2020.100399.

[42] K.P. Katuri, et al., Electroactive biofilms on surface functionalized anodes: the anode respiring behavior of a novel electroactive bacterium, Desulfuromonas acetexigens, Water Res. 185 (2020) 116284, https://doi.org/10.1016/j.watres.2020.116284.

[43] S.F. Ketep, A. Bergel, M. Bertrand, W. Achouak, E. Fourest, Lowering the applied potential during successive scratching/re-inoculation improves the performance of microbial anodes for microbial fuel cells, Bioresour. Technol. 127 (2013) 448–455, https://doi.org/10.1016/j.biortech.2012.09.008.

[44] V. Sapireddy, K.P. Katuri, A. Muhammad, P.E. Saikaly, Competition of two highly specialized and efficient acetoclastic electroactive bacteria for acetate in biofilm anode of microbial electrolysis cell, NPJ Biofilms Microbiomes 7 (1) (2021) 47, https://doi.org/10.1038/s41522-021-00218-3.

[45] A.M. Speers, G. Reguera, Electron donors supporting growth and electroactivity of geobacter sulfurreducens anode biofilms, Appl. Environ. Microbiol. 78 (2) (2012) 437–444, https://doi.org/10.1128/AEM.06782-11.

[46] M. Kokko, S. Epple, J. Gescher, S. Kerzenmacher, Effects of wastewater constituents and operational conditions on the composition and dynamics of anodic microbial communities in bioelectrochemical systems, Bioresour. Technol. 258 (2018) 376–389, https://doi.org/10.1016/j.biortech.2018.01.090.

[47] H. Wu, J. Gao, D. Yang, Q. Zhou, W. Liu, Alkaline fermentation of primary sludge for short-chain fatty acids accumulation and mechanism, Chem. Eng. J. 160 (1) (2010) 1–7, https://doi.org/10.1016/j.cej.2010.02.012.

[48] H. Sun, J. Li, M. Yang, Q. Shao, Influence of initial pH on anodic biofilm formation in single-chambered microbialelectrolysis cells, Pol. J. Environ. Stud. 28 (3) (2019) 1377–1384, https://doi.org/10.15244/pjoes/89503.

[49] A. Ghimire, et al., Bio-hythane production from microalgae biomass: Key challenges and potential opportunities for algal bio-refineries, Bioresour. Technol. 241 (2017) 525–536, https://doi.org/10.1016/j.biortech.2017.05.156.

[50] P.S. Bonanni, D.F. Bradley, G.D. Schrott, J.P. Busalmen, Limitations for current production in *Geobacter sulfurreducens* biofilms, ChemSusChem 6 (4) (2013) 711–720, https://doi.org/10.1002/cssc.201200671.

[51] Ashley E. Franks, Richard H. Glaven, Derek R. Lovley, Real-time spatial gene expression analysis within current-producing biofilms, ChemSusChem 5 (2012) 1092–1098, https://doi.org/10.1002/cssc.201100714.

[52] D. Sun, J. Chen, H. Huang, W. Liu, Y. Ye, S. Cheng, The effect of biofilm thickness on electrochemical activity of Geobacter sulfurreducens, Int. J. Hydrogen Energy 41 (37) (2016) 16523–16528, https://doi.org/10.1016/j.ijhydene.2016.04.163.

[53] K.M. Hernández-García, Modeling 3D current and potential distribution in a microbial electrolysis cell with augmented anode surface and non-ideal flow pattern, Biochem. Eng. J. 162 (2020).

[54] Z. Huang, L. Lu, D. Jiang, D. Xing, Z.J. Ren, Electrochemical hythane production for renewable energy storage and biogas upgrading, Appl. Energy 187 (2017) 595–600, https://doi.org/10.1016/j.apenergy.2016.11.099.